

Synergistic Effect of Photothermally Targeted NIR-Responsive Nanomedicine-Induced Immunogenic Cell Death for Effective Triple Negative Breast Cancer Therapy

Vellingiri Yasothamani, Laxmanan Karthikeyan, Selvaraj Shyamsivappan, Yuvaraj Haldorai, Dayakar Seetha, and Raju Vivek*

Cite This: *Biomacromolecules* 2021, 22, 2472–2490

Read Online

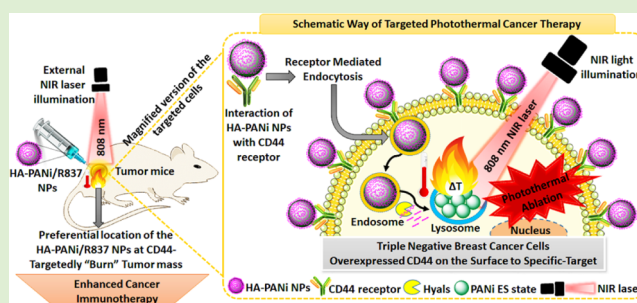
ACCESS |

Metrics & More

Article Recommendations

Supporting Information

ABSTRACT: Triple negative breast cancer (TNBC) is a breast cancer subtype. At present, TNBC patients do not have approved targeted therapy. Therefore, patients primarily depend on forceful systemic chemotherapy that has unavoidable harmful side effects, resulting in inadequate therapeutic outcomes and leading to a high mortality rate. Hence, there is an urgent need to develop targeted therapies for the TNBC populace. Developing a new nanotherapeutic approach of combinational therapy could be an effective alternative strategy. Therefore, we designed a combination of hyaluronan (HA)–polyaniline (PANi)–imiquimod (R837), denoted as HA-PANi/R837, nanoparticles (NPs) that exhibited a high extinction coefficient of $8.23 \times 10^8 \text{ M}^{-1} \text{ cm}^{-1}$ and adequate photothermal conversion efficiency (PCE) ($\eta = 41.6\%$), making them an efficient photothermal agent (PTA) that is highly beneficial for selective CD44-mediated photothermal ablation of TNBC tumors. Furthermore, co-encapsulation of R837 (toll-like receptor 7 agonist) immunoadjuvant molecules triggers an immune response against the tumor. The formed CD44-targeted HA-PANi/R837 NPs' selectivity incinerates the tumor under near-infrared (NIR)-triggered photothermal ablation, generating tumor-associated antigens and triggering R837 combination with anti-CTLA-4 for immunogenic cell death (ICD) activation to kill the remaining tumor cells in mice and protect against tumor relapse and metastasis. Our results demonstrated that novel HA-PANi/R837 NP-induced photothermal ICD achieved in CD44-targeted TNBC is a promising application.



1. INTRODUCTION

The World Health Organization reported that cancer is the main cause of deaths related to human diseases in the world every year and had estimated about 150 million deaths by 2020.^{1,2} Among the cancer types, deaths due to breast cancer (BC) are placed second after lung cancer deaths.³ Mostly, breast cancer is classified into three subtypes: hormone receptor-positive (ER+ and PR+), receptor human epidermal growth factor receptor 2 (HER2)-positive, and triple negative breast cancer (TNBC) (ER-, PR-, and HER2-).^{4–6} However, targeted therapy for the first two types of BC is possible due to the presence of specific receptors, whereas for TNBC, representing about 20% of all BC, targeted therapy remains challenging because of lack of targetable receptors; hence, chemotherapy is the first-line treatment option for TNBC.^{7–9} TNBC is also a highly aggressive BC, with a higher risk of early relapse and metastasis. At the same time, currently, TNBC patients do not have an approved targeted therapy and are most difficult to treat. Therefore, patients primarily depend on systemic chemotherapy that has certain adverse effects, resulting in poor therapeutic outcomes and leading to rapid drug resistance and a decrease in the overall survival rate. The

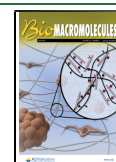
mortality rate of advanced-stage TNBC patients remains high; therefore, there is an urgent necessity to develop effective targeted TNBC therapy. Thus, new strategies of novel targeted therapy must have the advantage to overcome the aforementioned challenges for the treatment of TNBC patients.^{10–14}

Nowadays, nanotechnology research in medicine playing an active role in the development of highly potential nanomedicine is of great importance in addressing the unmet limitations of chemotherapeutics.^{15–17} Chemotherapy is the first treatment option for all types of cancers; however, existing limitations are mainly lack of tumor selectivity and insufficient target site accumulation, and adverse side effects ultimately lead to multidrug resistance (MDR).² Therefore, nanodrug

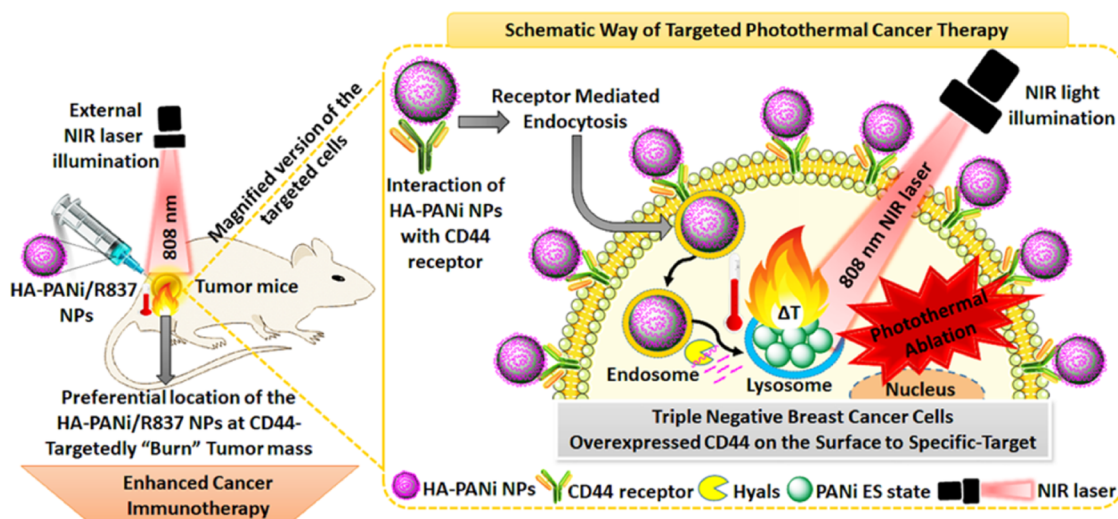
Received: February 23, 2021

Revised: May 5, 2021

Published: May 20, 2021



Scheme 1. Schematic Photograph Depicting the Multitasking Mechanisms of Combining NIR-Triggered HA-PANi NP-Loaded R837 for Highly Effective Cancer Photothermal Immunotherapy^a



^aHA-PANi/R837 NPs under NIR light facilitate CD44-targeted receptor-mediated effective photothermal destruction of tumors. Then, the preferential location of R837 further enhances the activation of the immune system-induced antitumor immunity.

delivery systems (NDDSs) have been developed and well explored within the nanoscale characteristic strategy for cancer treatment.^{18–21} Although NDDSs are promising, yet problems such as unsatisfactory drug loading, premature drug release, and insufficient release at the tumor site lead to low therapeutic efficacy.¹⁸ Thus, development of new nanotherapeutics has attracted much attention and can effectively increase the efficacy to overcome the chemotherapeutic drug challenges.

Photothermal cancer therapy (PTCT) is an emerging, noninvasive, localized cancer treatment method that can effectively induce tumor ablation using nanoscale particles as they liberate sufficient heat after light illumination.^{22,23} The efficiency of PTCT greatly depends on targeted light-responsive nanoparticles (NPs) that convert light to heat at the tumor site.^{8,24} Therefore, the utilization of organic photothermal agents (PTAs) has attracted increasing substantial attention because of their biocompatible properties that could be beneficial for safe and effective PTCT. The prime factor is that they do not affect normal tissues because of the thermal heat produced at the tumor site.^{23,25–27} Previously, we have designed organic PTAs for the selective ablation of tumors for PTCT without perturbation to the normal tissues.²⁸ Therefore, much effort is focused on near-infrared (NIR)-light-activated organic PTAs for cancer treatment.^{22,27,29} However, generating NIR-responsive organic NPs is highly challenging due to the fact that inorganic NPs, such as gold, sulfide, and platinum NPs, have a considerably favorable nanosystem. However, lack of biodegradability and potential long-term toxicity are a hindrance for clinical applications.^{23,30} However, the published clinical translation of AuroLasetherapy (AuroShell-PEGylated gold nanoshells) under an initial preclinical status and the clinical safety of this therapy are yet to be revealed (ClinicalTrials.gov Identifier: NCT02680535, NCT00848042, NCT01679470). Therefore, it is highly desirable to prepare PTAs with excellent photothermal conversion properties, satisfactory photothermal therapeutic efficacy, and superior biocompatibility.

Polyaniline (PANi) is the best example and the first reported organic conjugated PTA that is mostly utilized for biomedical applications, such as PTCT and photoacoustic imaging (PAI) of tumors.^{31–34} Studies reported that the NIR light absorption capacity of PANi is able to produce a considerable level of heat; thus, it could serve as an excellent photothermal heating agent. It further causes tumor cell irreversible damage followed by apoptosis, affecting its metabolism, DNA/RNA synthesis, protein denaturation, DNA repair, and membrane stability, which leads to tumor suppression and ablation.^{28,35–37} However, there are a few limitations, such as large size, lack of dispersibility, insolubility, poor tumor uptake, and lack of tumor cell targeting, that hamper its use for further clinical applications and make it highly challenging for targeted PTCT. Therefore, it is necessary to design and investigate effective PTAs that possess advanced features of selective activation in the tumor microenvironment (TMV), high photothermal conversion efficiency (PCE), specifically accumulating at the target tumor site, and biocompatible properties.

Previous attempts stated that hyaluronic acid or hyaluronan (HA) is water-soluble and consists of repeating units of *N*-acetylglucosamine and glucuronic acidic disaccharide in conjugation with water-insoluble drugs to improve solubility and acts as an active targeting ligand for biomedical applications.^{38,39} HA has multiple attractive properties not only as a major targeting ligand but also as being advantageous for its biocompatibility, nontoxicity, biodegradability, non-immunogenicity, and high levels of biosafety.⁴⁰ Moreover, HA could be successfully utilized for targeted drug delivery, prolonged blood circulation, improved physiological stability, and cytocompatibility with NPs.⁴¹ It is degraded by the action of hyaluronidases (Hylas) into tiny fragments in an enzyme-dependent manner after tumor endocytosis, due to the presence of a high level of Hylas present in several tumors. Moreover, HA enhances intracellular CD44-mediated uptake, thus improving the therapeutic outcome.⁴² In addition, particular features of HA, namely, polyanionic characteristics and high hydrophilicity, could also be used as an alternative for the frequently employed PEGylation to prolong the blood

circulation time and increase stability and biocompatibility when administered.⁴³ Therefore, it is proposed to enhance the PANi efficacy during PTCT and that of the immunotherapy combined system, and there has been rapid progress for the next generation of a combination treatment strategy. In 2018, Nobel Prize in Medicine was awarded for cancer immunotherapy, which has been an enormous boost and success in cancer treatment.^{44,45} However, activation of the immune system for the treatment of TNBC patients is still an active ongoing clinical study.

Therefore, developing a PANi-based combination of synergistic photothermal immunotherapy remains relatively unexplored. Despite this circumstance, we have combined HA-PANi-loaded imiquimod (R837, Food and Drug Administration (FDA)-approved immunomodulator), an immunoadjuvant. R837 is a toll-like receptor 7 agonist, which is co-encapsulated on the NP surface and denoted as HA-PANi/R837 NP. Therefore, HA-PANi/R837 NP-based PTCT combined with anti-CTLA-4 therapy produced immunogenic cell death (ICD) to kill the remaining tumor cells in treated mice. This in turn demonstrates the active immune-memory effect to protect the mice from tumor relapse. To explore the combined photothermal immunotherapy application in TNBC therapy, the present study is one of the first attempts of a specifically developed tumor-targeted PANi-based immunonanomedicine with high potential for the development of efficient TNBC therapy (Scheme 1).

2. MATERIALS AND METHODS

2.1. Materials Required. All of the chemicals, aniline, ammonium peroxydisulfate (APS), citric acid (CA), hyaluronic acid (HA), dichloromethane, and sodium dodecyl sulfate (SDS), used were of pure analytical grade (99.99%). 3-(4,5-Dimethylthiazol-2-yl)-2,5-diphenyltetrazolium bromide (MTT) and 2',7'-dichlorofluorescein diacetate (DCFH-DA) were used according to the manufacturer's instructions. All other chemicals and reagents were of analytical grade. Ultrapure deionized water (DW) was used in this study.

2.2. Preparation of HA-PANi/R837 NPs. The PANi NPs were prepared by a process of chemical oxidative polymerization.^{46,47} In a typical method, comparing the targeted and the nontargeted effect, we selected the acid for preparing PANi NPs. HA (1.63 g) and aniline (0.65 g) were mixed in 30 mL of deionized water. The mixture was stirred well at room temperature. Subsequently, 1.60 g of APS in deionized water (70 mL) was slowly added dropwise. The reaction mixture was stirred for another 24 h, and a dark-green precipitate was formed. The top layer of the as-prepared HA-PANi NP product was collected and centrifuged at 2500 rpm for 10 min and then the precipitates were collected. After warming to room temperature, the resulting precipitate was filtered and washed with a small amount of water to remove the nonreacted chemical substance, inorganic salts, possible ions, remnant oligomers, and byproducts. Then, it was dried in vacuum to obtain a dark-green powder, which was the first piece of evidence of NPs in the form of a conductive emeraldine salt (ES), further confirmed by it absorbing NIR light. The HA-PANi/R837 NPs were obtained by co-encapsulating R837 with the NPs; first, R837 was dissolved in dimethyl sulfoxide (DMSO) with a 4 mg/mL concentration. Under a nitrogen atmosphere at room temperature, mechanical stirring was continued with 0.5 mL of NPs, and 0.5 mL of R837 was injected dropwise into 10 mL of deionized water. Subsequent ultrasonic treatment of the emulsion was carried out, and the emulsion was further stirred for 4 h to evaporate the organic solvent. Then, the final product was washed three times via centrifugation for 10 min at 6000 rpm and further dialyzed with a molecular weight cutoff (MWCO) of 7 kDa against DW for 24 h and was further denoted as HA-PANi/R837 NPs.

2.3. Experiments on Loading and Releasing of R837. The R837 solution was prepared in DMSO with a 1 mg/mL concentration and then diluted in water to standard solutions of 2.5, 5, 7.5, and 10 $\mu\text{g/mL}$. The UV absorption spectra of the R837 solution with different concentrations at 322 nm were measured. According to R837 absorbance, a linear standard curve was obtained. Then, the encapsulation and loading efficiencies of R837 were also calculated from the UV absorption spectra against the standard curve. Next, the R837 release from the NPs was measured under the illumination of a NIR laser and then centrifuged to obtain the supernatant. The released percentage can also be calculated from the absorbance at 322 nm according to the standard curve.

2.4. Characterization of NPs. UV-vis-NIR absorption spectra analysis was performed using visible wavelength over the range from approximately 250 to 900 nm. Absorption spectra were recorded at room temperature using a UV-vis spectrophotometer (TestRight Nanosystems, Pvt. Ltd., India). Dynamic light scattering (DLS) analysis of the particle size along with its polydispersity was performed using a particle size analyzer (90 Plus Particle Size Analyser, Brookhaven Instruments Corporation). The particle size was determined by measuring the time-dependent fluctuation of the scattering of laser light by the NPs undergoing Brownian motion. Briefly, the samples of the NP stock solution were stepwise extruded through 0.22 μm membranes after ultrasonic vibration for 5 min and analyzed using a Brookhaven A8530 apparatus in triplicate at 25 $^{\circ}\text{C}$. ζ -Potential analysis of the NPs used to determine the surface charge of the prepared NPs was performed using a ζ -potential analyzer (90 Plus Particle Size Analyzer, Brookhaven Instruments Corporation, using Zeta plus software) at 25 $^{\circ}\text{C}$ in ultrapure water. The NP solution was diluted using deionized water after being filtered. Then, the prepared NP dispersion was determined before measurement. Next, ζ -potential was calculated based on the direction and the velocity of particles under the influence of a known electric field. Transmission electron microscopy (TEM) analysis was used to identify the morphology of the NPs (JEM-2100, JOEL). Fourier transforms infrared (FT-IR) spectroscopy analysis of NPs was performed using a Nicolet 5700 instrument (Nicolet Instrument, Thermo Company) and the KBr pellet method. Each KBr disk was scanned over a wavenumber region of 500–4000 cm^{-1} .

2.5. Photothermal Performance of NPs. To measure the photothermal performance of the as-synthesized NPs, an 808 nm NIR laser was employed whose light was to be delivered perpendicularly through a quartz cuvette containing an aqueous dispersion (0.5 mL) of NPs with a concentration of 0.1 mg/mL, and water was used as a control. The NIR laser light source had a power of 1 W/cm^2 under the 808 nm semiconductor laser device with a 5 mm diameter laser module. The temperature was measured using a thermocouple thermometer, which was inserted into the aqueous dispersion perpendicular to the path of the laser light.

The photothermal conversion efficiency (PCE) of the NPs was determined according to a reported method.³¹ To measure the PCE (η), the NP aqueous dispersion samples were exposed to the 808 nm NIR laser (1 W/cm^2) for 5 min, and then the laser was shut off. The heating and cooling temperature trends of the samples were recorded using a temperature gauge. The calculation of the molar extinction coefficient was according to eq 1

$$\epsilon = \frac{AV_{\text{NPs}}\rho N_{\text{A}}}{LC} \quad (1)$$

where ϵ is the molar extinction coefficient, A is the wavelength of 808 nm NP absorption, V_{NPs} (in cm^3) is the average NP volume, ρ is the NP density, N_{A} is Avogadro's constant, L is the path length (1 cm), and C (in g/L) is the weight concentration of the NPs.

Photothermal conversion efficiency (η) was determined using eq 2

$$\eta = \frac{hA\Delta T_{\text{max}} - Q_{\text{S}}}{I(1 - 10^{-A})} \quad (2)$$

where η is the PCE from light to heat energy, h is the heat transfer coefficient, A is the surface area of the container, ΔT_{max} is the

temperature change at the maximum steady-state temperature, Q_s is the heat associated with light absorbance of the solvent, which is measured using pure water without NPs, I is the laser power, and A_λ is the absorbance of the NP wavelength of 808 nm.

To obtain the value of hA , θ was introduced, which is defined as the ratio of ΔT and ΔT_{\max} by eq 3

$$\theta = \frac{\Delta T}{\Delta T_{\max}} \quad (3)$$

where ΔT is the temperature change, which is defined as $T - T_{\text{sur}}$ (T and T_{sur} are the surrounding solution temperature and the ambient temperature, respectively). Finally, hA was determined by eq 4

$$hA = \frac{mC_p}{\tau} \quad (4)$$

where τ is the slope of the linear time data from the cooling period versus $\ln \theta$. m and C_p are water mass and heat capacity, respectively.

To further evaluate the photothermal stability of NPs, a periodic laser on/off control with 808 nm NIR light and a power density of 1 W/cm² was used. The temperature changes were recorded during the five cycles of on/off NIR laser irradiation. Furthermore, UV–vis–NIR absorbance spectra were used to study the photothermal stability of NPs. Then, the UV–vis–NIR absorbance spectra analysis of indocyanine green (ICG) was compared with that of the NPs to measure with or without five on/off cycles of irradiations.

2.6. Studies on the Cellular Uptake of NPs. To investigate the intracellular CD44-mediated endocytic uptake characteristics of NPs, we seeded 5×10^4 cells into a 35 mm confocal dish and incubated them overnight to allow for the cells to adhere firmly to the bottom of the dish. Subsequently, the cells were washed thrice with phosphate-buffered saline (PBS), and 1.5 mL of the NP suspension (50 $\mu\text{g}/\text{mL}$ in Dulbecco's modified Eagle's medium (DMEM)) was added to the dish and incubated at 37 °C for various times. After washing thrice with PBS to remove residual NPs and dead cells, the cells containing NPs were cell-sliced to observe the endocytosis-mediated cellular uptake process, which was monitored using TEM imaging.

2.7. *In Vitro* Cytotoxicity Assay. MDA-MB-231 cells were cultured in standard cell media recommended by ATCC and obtained from the National Centre for Cell Science (NCCS), Pune, and maintained in DMEM containing 10% fetal bovine serum (FBS) and 1% penicillin–streptomycin solution supplemented with nonessential amino acids. Cells were cultured at 37 °C in a humidified atmosphere containing 5% CO₂ in a CO₂ incubator, and $\sim 1 \times 10^4$ cells/wells were seeded into 96-well tissue culture plates and incubated for 48 h. Cancer cells were treated with a series of NP concentrations (0, 0.25, 0.50, 0.75, 1.0 mg/mL) as determined for the *in vitro* test. The treated cells were incubated for 24 h for cytotoxicity analysis. The cells were then subjected to the standard MTT cell viability assay. The experiment was repeated three times.

2.8. Lactate Dehydrogenase (LDH) Measurement Assay. The LDH leakage assay was performed using a homogeneous membrane integrity assay kit following the manufacturer's protocol. In this experiment, cells were incubated with different concentrations of NPs for 24 h. The positive control was obtained by incubating cells with 1% Triton-X-100 for 30 min. The cell-free medium was used as the medium background. The measurement was performed using a microplate reader.

2.9. Intracellular Reactive Oxygen Species (ROS) Assay. The intracellular ROS level was detected by DCFH-DA staining. MDA-MB-231 cells were first exposed to NPs for 24 h. For fluorescence microscopy imaging, the cells were washed three times with DMEM and incubated with 10 $\mu\text{mol}/\text{L}$ DCFH-DA for 20 min. After washing with PBS twice, the cells were observed using a fluorescence microscope (Olympus, Japan). For fluorometric analysis, the fluorescent MDA-MB-231 cells were observed at excitation and emission wavelengths of 488 and 530 nm, respectively. The MDA-MB-231 cells without exposure to NPs were used as the negative control, and the MDA-MB-231 cells exposed to 100 μM H₂O₂ were used as the positive control.

2.10. *In Vitro* Photothermal Ablation. To study the photothermal ablation effect on tumor cell death, the MDA-MB-231 cells were incubated in 96-well tissue culture plates at a density of 5×10^3 cells/well in DMEM complete medium for 24 h. Then, the medium was replaced with 100 μL of fresh DMEM complete medium containing various formulations of NPs with concentrations of 0.25–1.0 mg/mL, and the cell samples were exposed to an 808 nm near-infrared laser with a power density of 1 W/cm² for 5 min. After incubation, each well was washed and 20 μL (5 mg/mL) of MTT solution was added. The plates were incubated for 4 h in an incubator; next, the solution was removed, and 200 μL of DMSO was added. Then, the plates were shaken on a table concentrator for 10 min. Finally, a microplate reader was used to detect the absorbance at 570 nm. The cell viability is determined using the following equation: cell viability (%) = (mean of abs. value of treatment group/mean abs. value of control) \times 100%.

2.11. Apoptotic Fluorescence Imaging Analysis. Calcein acetoxymethyl ester (calcein-AM) and propidium iodide (PI) were added to the cells after incubation of NPs under NIR light, and the final concentrations of calcein-AM and PI used were 2 and 4 μM , respectively. After 45 min of incubation at 37 °C, the cells were imaged using an Olympus confocal imaging system (Olympus FV100; Olympus Corporation) and excitation wavelengths of 488 nm (calcein-AM) and 533 nm (PI).

2.12. Flow Cytometry Analysis. For the detection of apoptosis in cancer cells, the cells were stained with annexin V–fluorescein isothiocyanate (FITC) and propidium iodide (PI). In brief, the cells were pretreated with NPs. The treated cells were suspended in 200 mL of binding buffer; then, 10 mL of annexin V–FITC and 5 mL of PI were added to the suspension, followed by incubation for 15 min in the dark at room temperature. Subsequently, 300 mL of binding buffer was added to the cell suspension, and the cells were analyzed using flow cytometric analysis.

2.13. Hemolysis Assay. A hemolysis assay was performed to determine the *in vivo* blood biocompatibility of NPs. Briefly, red blood cells (RBCs) were obtained by removing the serum from human blood after washing with 0.9% saline and centrifuging at 4000 rpm five times to obtain a clear supernatant. Subsequently, blood RBC cells were diluted with the PBS solution. Next, 0.3 mL of the diluted cell suspension was then mixed with 1 mL of PBS (as a negative control), 1 mL of deionized water (as a positive control), and 1 mL of NP suspensions with varying concentrations. The samples were shaken for several minutes and then kept steady for 2 h. Finally, the mixtures were centrifuged at 4000 rpm, and the absorbance of the upper supernatants was measured using UV–vis spectroscopy. The hemolysis percentage was calculated.

2.14. Ethics Statement for *In Vivo* Experiments. All of the *in vivo* animal experiments were conducted as per the guidelines of the Institutional Review Board. Animal experiments using mice were performed after obtaining prior approval of the specialized institutional animal ethical committee (IAEC) and adhering to the strict guidelines and recommendation of the committee for the purpose of control and supervision of experiments on animals (CPCSEA), constituted by the Animal House Division. The experiments and the handling of the animals were carried out as per the guidelines of CPCSEA. The procedures conformed to the guidelines regarding the ethical use of animals. Animal usage was officially permitted by the IAEC, and *in vivo* animal experiments were performed in agreement with the IAEC of the university, and all of the balb/c mice of 20 ± 2 g were procured from the Kerala Veterinary and Animal Sciences University, Animal Centre, and maintained in suitable experimental conditions, such as at room temperature of 24 ± 2 °C and 40–60% relative humidity while on a regular 12 h light/dark cycle. The experimental animals were acclimatized for a minimum period of 3 days prior to the *in vivo* experiment.

2.15. Photothermally Ablated Tumors for Immune System Activation. Animal experiments were carried out using female balb/c mice (4–5 week old), which were acclimatized at 25 °C and 55% humidity under natural light/dark conditions approved by the ethical committee. The 4T1 cells were used for the mice TNBC tumor

animal model and were maintained in DMEM. Mice were anesthetized *via* intraperitoneal injection of 45 mg/kg pentobarbital sodium, and then subcutaneous tumors were established by injection of 1×10^6 cells/mL cells suspended in 200 μ L of PBS into mice. After 15 days, when the tumor grew to 5–7 mm in diameter, the animals were randomized and selected for various treatment groups and photothermal studies were performed. The mice were randomly divided into four groups ($n = 5$ for each group) and treated with the following experimental conditions. (1) Blank saline group: no injection of HA-PANi/R837 NP solution and without 808 nm laser exposure. (2) Control group: no injection of HA-PANi/R837 NPs (laser only). (3) Treatment of HA-PANi/R837 NPs without 808 nm laser exposure. (4) Test group: PBS solution of HA-PANi/R837 NPs was intratumorally injected into the mice, which were exposed to the 808 nm laser light (1 W/cm^2) for 5 min (HA-PANi/R837 + NIR laser). The local maximum temperature was recorded on an infrared thermal imaging camera (Testo, Germany). After NP irradiation, anti-CTLA-4 was intravenously (*i.v.*) injected with a dose of 10 μ g per mice. After these treatments, the tumor size was measured using a caliper each day and calculated as volume = (tumor length) \times (tumor width)²/2. Relative tumor volumes were calculated as V/V_0 (V_0 is the tumor volume when the treatment was initiated). The body weights of the mice were also recorded each day, and the results were plotted as a function of time. An *in vivo* blood circulation half-life measurement experiment was performed, where the mice ($n = 3$) were intravenously injected with NPs in PBS. At various time points up to 24 h postinjection, 15 μ L of mice blood was collected and dissolved in 985 μ L of physiological saline containing 10 mM ethylenediaminetetraacetic acid (EDTA) as an anticoagulant. The concentration of the sample was determined. The curve of the blood circulation half-life was fitted based on a single-compartment pharmacokinetic model.

2.16. Histology and Hematological Examination. Histology analysis was performed on the 14th day after treatment. The typical heart, liver, spleen, lung, and kidney tissues of the mice in the different treatment groups were isolated. Then, the organs were dehydrated using buffered formalin, ethanol with different concentrations, and xylene and then embedded in liquid paraffin. Next, the organ tissues were sliced to 3–5 mm and stained with hematoxylin and eosin (H&E) and examined using a microscope. Blood was collected from the orbital sinus by quickly removing the eyeball from the socket with a pair of tissue forceps. Six important hepatic indicators (TBIL, total bilirubin; GLO, globulin; ALT, alanine aminotransferase; AST, aspartate aminotransferase; GGT, glutamyl transpeptidase; TBA, total bile acid) and four indicators for kidney functions (GGT, glutamyl transpeptidase; UA, uric acid; UREA, urea; CRE, creatinine) were measured. Blood smears were prepared by placing a drop of blood on one end of a slide and using another slide to disperse the blood along the length of the slide. The slide was left to air-dry, after which the blood was stained with hematoxylin and eosin (H&E). Upon completion of blood collection, the mice were sacrificed. For H&E-stained tissues, the main organs of interest (heart, liver, spleen, lung, and kidney), were harvested from the mice. The tissues were fixed in 10% formalin, dehydrated with ethanol, embedded in paraffin, sectioned, and stained with H&E. The histological sections were observed under an optical microscope. Three repeated experiments were performed for histology and hematology studies.

2.17. Ex Vivo Analysis of T Cells in Different Groups. In this *ex vivo* analysis, immune cells in tumors were collected from post-treatment tumor mice in different groups. Briefly, collected tumor tissues were cut into small sizes in a glass homogenizer containing PBS (pH 7.4) with 2% heat-inactivated FBS. Then, a single-cell suspension was prepared by the gentle pressure of the homogenizer without addition of the digestive enzyme. Finally, cells were stained with fluorescence-labeled antibodies after the removal of red blood cells (RBCs) using the RBC lysis buffer. For the dendritic cell (DC) maturation experiments, DCs were treated with saline, NIR, HA-PANi/R837 NPs, and HA-PANi/R837 NPs with NIR. Alternatively, residues of tumor cells after photothermal ablation with HA-PANi/R837 NPs were also added into the DC culture using a transwell

system. Cytotoxic T lymphocytes (CTLs) and helper T cells were analyzed according to the standard protocols. The single-cell suspension of the lymph nodes was also prepared using the same protocol. All of the antibodies were diluted 200 times before they were used for these study experiments.

2.18. Cytokine Detection. All of the serum samples were isolated from the various post-treatments of mice and then diluted for further analysis. Tumor necrosis factor (TNF- α), interferon γ (IFN- γ), and Interleukin (IL)-6 were analyzed using enzyme-linked immunosorbent assay (ELISA) kits according to the manufacturer's protocols.

2.19. Immunogenic Cell Death Marker Detection. The level of extracellular release of adenosine 5'-triphosphate (ATP) was measured using an ATP assay kit. Briefly, tumor cells were seeded in six-well cell culture plates and incubated with NPs for 3 h with different treatments. The culture supernatant was collected and centrifuged at 12 000g for 10 min. Then, the supernatant was transferred into tubes to test for ATP release. The luminescence from 20 μ L of the sample was assessed using a multiscan spectrum (Thermo Fisher Scientific & Co.) together with 100 μ L of ATP detection buffer. Then, the ATP level was normalized according to the protein concentration. Another ICD marker assay for HMGB1 release was also carried out using ELISA in tumor cells. Cells were seeded at 3×10^6 cells per well in six-well plates. After 24 h of incubation, cells were treated with NPs with different treatments for 3 h. HMGB1 expression was detected using an ELISA assay kit.

2.20. Statistical Analysis. The statistical analysis was performed with the Statistical Program for Social Sciences (SPSS) software as needed. All data were expressed as means \pm standard deviation (SD), and a statistically significant and a highly significant difference considered to be present at $P < 0.05$ and < 0.01 are shown by asterisks in the figures, except, as mentioned, all assays were performed repeatedly in independent experiments.

3. RESULTS AND DISCUSSION

3.1. Preparation of HA-PANi/R837 NPs and Characterization. To synthesize CD44-targeted HA-PANi/R837, nanotherapeutics were prepared to achieve selective photothermal ablation and targeted antitumor immune activation in TNBC.^{28,46} The proposed mechanism of HA with PANi by the electrostatic interaction between negatively charged HA and positively charged PANi and further co-encapsulated with R837 was used. The nanocomposite was synthesized according to a previously well-established method.⁴⁶ The regression equation is determined by the absorbance at 322 nm *versus* the feeding concentration of R837 molecule encapsulation (Figures S1 and S2). Furthermore, excess unloaded molecules were removed by centrifugation at 14 000 rpm for 10 min and then washed three times with PBS. At the end of the optimized loading condition, the loading capacity of R837 onto the HA-PANi NPs was measured and determined to be $\sim 1\%$ (Figure S3a). Finally, R837 was successfully loaded in the NPs and the final nanocomposite of HA-PANi/R837 NPs was obtained and used for further experiments. Especially, HA is used as a PANi doping acid for the transition of the NIR responsible emeraldine salt (ES-semioxidized and protonated form) state that can be photoexcited to generate considerable photothermal heat. Moreover, HA plays a dual role in PANi doping and active targeting of CD44 receptors that are overexpressed at TNBC tumor cells. Furthermore, the appearance of a clear dark-green color in the dispersed NPs stored in PBS and DMEM was noted, and no precipitation was observed after a week. Hence, NPs maintained nearly constant and enhanced stability (Figure S5a). Therefore, the prepared composite NPs showed good stability in various buffers and were also found to be stable in aqueous dispersion for at least a week without any noticeable aggregation.

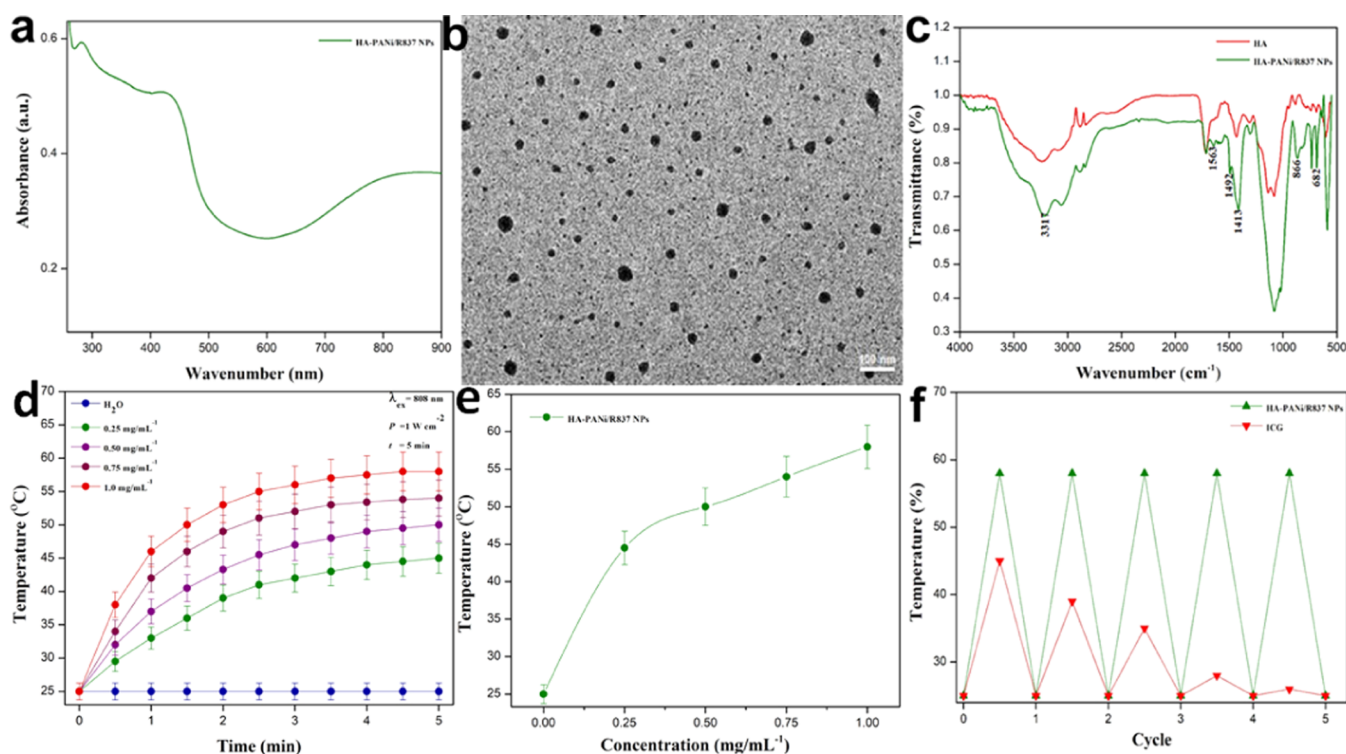


Figure 1. Synthesis and characterization of NPs. (a) UV–vis–NIR confirmative absorption spectra of HA-PANi/R837 NPs. (b) Representative morphological TEM image of HA-PANi/R837 NPs. (c) FT-IR confirmative spectra of HA and HA-PANi/R837 NPs. (d) Photothermal response of different concentration-dependent (0.25–1 mg/mL) HA-PANi/R837 NPs under illumination for 5 min with a NIR laser (808 nm, 1 W/cm²). (e) Final temperature curve of the corresponding HA-PANi/R837 NP dispersion after 5 min of laser illumination; the data were obtained from (d). (f) Photostability of the HA-PANi/R837 NP dispersion compared with ICG under continuous laser illumination (808 nm, 1 W/cm²) with repeated five on/off cycles. The temperature changes of free ICG and NPs in aqueous solution for different time points. The results are presented as means \pm SD ($n = 3$).

The NPs were primarily confirmed by UV–vis–NIR absorption spectra for their characterization before being used for PTCT because of the NIR light absorption properties of NPs. In Figure 1a, the NPs attained a maximum UV–vis–NIR absorbance with two main bands at 430 and above 800 nm (Q-band). A clear observation of assigned $\pi \rightarrow \pi^*$ benzene rings for transition and charge transfer between quinoid and benzenoid rings was noted.⁴⁷ Absorption bands at 430 nm indicate the successful HA doping on PANi NPs. In particular, NPs showed a considerable red shift toward the NIR region with the central broad absorption above 800 nm. Therefore, UV–vis–NIR results confirmed that NPs showed extensively high NIR absorption. The UV–vis spectrum of HA and R837 alone was determined (Figure S3b). This change was attributed to the actuality of PANi in the ES state of PANi doping, which induces the association of electrons and decreases the excitation-energy level. Therefore, NPs exhibited the strongest absorption in the NIR-I biological window; moreover, the corresponding mass molar extinction coefficient (ϵ) at 808 nm was calculated and found to be around $8.23 \times 10^8 \text{ M}^{-1} \text{ cm}^{-1}$, which is higher than that of other PTAs, such as AuNPs, CNT, and CuS.⁴⁸ It is noticed that the practically no observable fluorescence emission from NPs upon excitons' arrival to the ground-state level of nonradiative decay is the main pathway for excited-state deactivation to generate heat.⁴⁹ Therefore, NIR red-shifted NPs have the ability to act as a typical photothermal coupling agent that reacts at suitable adsorption of NIR light in the range of 700–900 nm without causing any harmful damages to blood or normal tissue. Thus,

we confirmed that NPs are well-suited to become a potential promising PTA with the ability to generate heat under NIR light irradiation for tumor cell ablation.

During subsequent characterization, the transmission electron microscopy (TEM) morphometric study revealed the morphology and dispersion of NPs. Therefore, the TEM image clearly displayed a uniformly dispersed spherical nanostructure with a diameter less than 100 nm (Figure 1b). The TEM morphological size distribution also exhibited the mean size of the HA-PANi/R837 NPs. Therefore, the aforesaid facts confirmed the spherical nanostructure with a highly aqueous stable system, which profits from the outstanding hydrophilic nature of HA that exists in the cationic PANi backbone to avoid aggregation. Thus, the morphological nanostructures and the dispersion uniformity of the particles are suitable for further biological applications. Dynamic light scattering (DLS) of the NPs reveals size distribution ranging from 100 to 200 nm and ensures escape filtration by liver and spleen. The sub-100 nm wavelength could easily penetrate well within the tumor.⁴⁹ Thus, DLS results showed the HA-PANi/R837 NP hydrodynamic size to be ~ 79 nm, and particles were slightly polydispersed.

Furthermore, the surface charge of NPs is also an important parameter that has to be taken into account because our aim is to increase the specific cellular internalization process.²¹ Generally, positively charged NPs have better internalization capacity by the normal and cancer cells due to the interaction with the negatively charged cell membrane surface. Especially, the tumor cell plasma membrane has a huge number of

negatively charged components (e.g., phosphatidylserine or sialic acid); thus, it consequently promotes the uptake of positively charged NPs. However, positively charged NPs have a higher rate of nonspecific uptake and facilitate endosomal discharge in the mass of tumor cells, whereas when the NP surface is conjugated with the targeting moiety, it enhances the specific endocytic uptake. Therefore, owing to these facts, the NPs, which have a negative ζ -potential value of -26.5 mV, were measured to consider the positively charged PANi surface decorated with negatively charged HA, which is more suitable for specific-cancer receptor-targeted therapeutic applications. Therefore, compared to positively charged NPs, negatively charged NPs have good biocompatibility, reduced protein adsorption and antigenicity, and long-time circulation half-life.¹⁸ Then, the synthesized NPs were characterized using Fourier-transform infrared (FT-IR) spectroscopy, which is generally used to confirm the molecular identification of combined substances. In Figure 1c, FT-IR spectra revealed that the chemically combined structures of HA-PANi/R837 NPs observed characteristic conformation and had absorption bands of NPs at 866 cm^{-1} (C–H out-of-plane bonding in the benzenoid ring) and 682 cm^{-1} (C–H strong aromatic bond); bands at 1563 and 1492 cm^{-1} indicated the quinoid and benzenoid (C=N, C=C) rings. Then, the peaks authenticated the presence of PANi bands at 1431 cm^{-1} assigned to the carboxylate HA stretching, and it shifted to 1413 cm^{-1} . This is found to be due to the interaction of carboxyl HA groups with the PANi ammonium group. The main peaks of R837 were at 3300 , 2500 , 1670 , and $650\text{--}900\text{ cm}^{-1}$, which disappeared in the NP spectra. The presence of the NH stretching peak of 1° amine in R837 at 3317 cm^{-1} was observed in the NPs. Furthermore, the results also indicated the HA and R837 existence in the combined form of NPs. Successively, the FT-IR conformational features of R837-loaded HA-decorated PANi NPs were obtained. All of these typical characteristic peaks are shown in the range of $4000\text{--}500\text{ cm}^{-1}$. The most important bands were assigned to provide solid evidence for the C=N and C=C stretching vibration, confirming the presence of PANi quinoid and benzenoid rings. These FT-IR bands are well in agreement with previous reports.^{28,46} The results clearly demonstrated that our abovementioned hypothesis of the electrostatic interaction process is the main feature of combined NPs.

3.2. Photothermal Performance and Stability of NPs.

These NIR-responsive nanotherapeutic agents show potential in medicine because of their disease-specific targeting functions, as well as high precision and negligible invasiveness.⁵⁰ Fascinatingly, the nanomaterials illuminated with NIR light can convert light to heat that incinerates the tumor; thus, it does not affect the surrounding normal cells, providing a specific heat therapy to “burn” tumor cells.⁵¹ Therefore, we investigate the photothermal potential of NPs, and the photothermal conversion efficiency (PCE) index (η) value was calculated due to a considerable unambiguous amount of photon energy that was directly delivered into the tumor mass without any systemic side effects, which is the most essential attribute for highly efficient PTCT. The UV–vis–NIR absorption capacity of NPs highly encouraged us to further explore NIR-light-responsive photothermal conversion properties. Furthermore, we aimed to test the PCE experiment under 808 nm laser light illumination to provide strong evidence for their potential use as NIR-I therapeutic agents in clinical applications.²⁸ For further corroboration, the PCE of the NPs

used as a PTA up to 1 mg/mL solution concentration was exposed at 808 nm NIR laser light illumination with a 1 W/cm^2 power density for 5 min (Figure 1d). Various (0.25, 0.50, 0.75, and 1.0 mg/mL) concentration-dependent temperature-increasing trends noticed in NPs in aqueous dispersion were very clearly observed under NIR light illumination. Most importantly, our NPs exhibited great concentration-dependent PCEs and high stability without any significant decrease of the optical absorbance after continuous exposure to the NIR laser for a long period of time. At the same time, as a control, pure water was used for the photothermal assessment. While thermal signals in aqueous NP dispersion successively increased with the increase of the NIR illumination at different time intervals, the DI water exhibited no noticeable changes in temperature, indicating that no signals of PCE occur because there is no significant temperature change when exposed to NIR light illumination in water, and the temperature was maintained at $25\text{ }^\circ\text{C}$ after 5 min. However, the temperature of the NPs gradually increased; at the end point, the temperature sharply increased above $55\text{ }^\circ\text{C}$ within 5 min. The final temperature of each concentration, which corresponds to the NP dispersions after 5 min of NIR laser irradiation, is shown in Figure 1e. It is very important to note that NPs increased high temperature profile of light to heat conversion. Additionally, we have also quantitatively calculated the photothermal conversion (η) profiles of NPs based on previous reports.^{31,32,34} It has been well illustrated that temperatures above $48\text{ }^\circ\text{C}$ result in immediate coagulative necrosis and irreversible tumor cell death, and also the estimated PCE of HA-PANi/R837 NPs is 41.6%, which is higher than those of previously reported systems such as IR1048-MZ (20.2%), dopamine–melanin central nervous systems (CNSs) (40%), polypyrrole@Fe₃O₄ (39.15%), black phosphorus quantum dots (28.4%), and Au nanorods (21%).^{22,50} Therefore, it has also been well noticed that the NP dispersion exhibited good PCE at 808 nm with a higher mass extinction coefficient, which has good photothermal conversion ability under the appropriate time points with different power densities (Figure S4). It possibly leads to good photostability and a potential PTA for cancer treatment. Therefore, the NIR-responsive photothermal performance of NPs was again preferred for the following experimental study.

Next, we evaluated the photothermal stability of nanomaterials, which is also one of the essential parameters. Therefore, to further investigate the photothermal stability of the NPs, the NP samples were illuminated using 808 nm NIR light for 5 min and then turned off. The samples are allowed to cool to room temperature, and then the off/on cycle is repeated up to five times. NPs were compared with the FDA-approved ICG photosensitizer, which is widely used for clinical phototherapy.²² Therefore, after the five off/on cycles, NPs still maintain the efficiency of photothermal performance, whereas ICG fails to maintain the photothermal effect typically under the same conditions (Figure 1f). The temperature of NPs still reached above $52\text{ }^\circ\text{C}$ at the end of five cycles. However, it is clearly evidenced that the NIR light-absorbing capacity of NPs did not change during this process; at the same time, ICG molecules totally disappear at the completion of five cycles on rapidly decreasing the temperature. Notably, after the five cycles of NIR light illumination, there is no considerable change that is noticed in the narrow size distribution, which is significantly maintained by NPs. Henceforth, the aforementioned investigation results confirmed that the highly stable

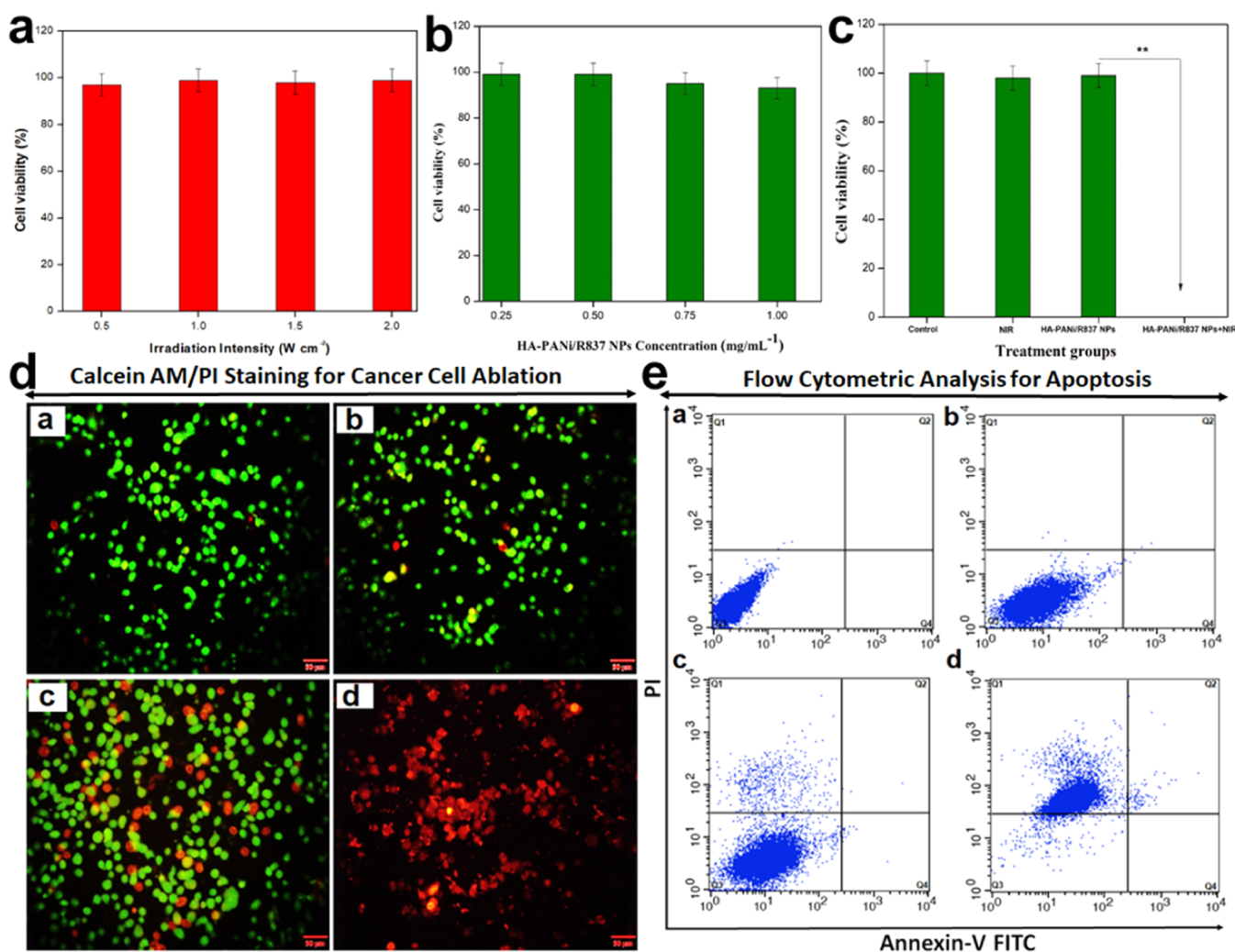


Figure 2. *In vitro* cell experimental studies. (a) Relative cell viability of MDA-MB-231 cells treated with different laser powers of 0.5, 1.0, 1.5, and 2.0 W/cm². (b) MDA-MB-231 cells after being incubated with various concentrations of 0.25, 0.50, 0.75, and 1.0 mg/mL HA-PANi/R837 NPs for 24 h. (c) Relative viability test of MDA-MB-231 cells after NP-induced photothermal ablation being treated with the highest biocompatible concentration of 0.50 mg/mL HA-PANi/R837 NPs with NIR laser illumination of 808 nm with a power of 1 W/cm². Student's *t*-test, **compared with the control group, $P < 0.01$. (d) Fluorescence images of calcein-AM/PI dual-stained MDA-MB-231 cancer cell ablation compared with (a) untreated control cells, (b) HA-PANi/R837 NPs without light, (c) 808 nm NIR alone, and (d) cells treated with 0.50 mg/mL HA-PANi/R837 NP incubation after being exposed to the 808 nm laser at a 1 W/cm² power density. Live/dead staining shows dead cells in red and viable cells in green. Scale bars, 50 μ m. (e) Quantitative Apoptosis analysis of MDA-MB-231 cells by staining with Annexin V–FITC and PI: (a) untreated control cells, (b) HA-PANi/R837 NPs without light, (c) 808 nm NIR alone, and (d) cells treated with 0.50 mg/mL HA-PANi/R837 NP incubation after being exposed to the 808 nm laser at a 1 W/cm² power density.

photothermal performance of NPs and their stability potential acted as effective photothermal conversion nanomaterials for further *in vitro* and *in vivo* PTCT treatment.⁴⁶ In contrast, the fluorescence intensity of ICG completely disappeared after irradiation under the same conditions (Figure S5b). The photothermal stability curve was expressed after five cycles of 808 nm NIR laser illumination where there was a decreasing level of photothermal fluorescence intensity of free ICG compared with NPs. However, the same normalized intensity was maintained by our NPs. This high photostability is a particular feature and an advantage of organic nanomaterials over conventional organic dyes.²²

3.3. TEM Analysis of the Intracellular Uptake of NPs.

To address the nontargeting limitation of NPs, a HA tumor-specific moiety that could specifically bind to the CD44 receptor, which is overexpressed in TNBC cells, was introduced on the NP surface. It enables to achieve the active

targeting uptake of NPs. We investigated the cellular endocytic uptake of the NPs; the targeting moiety of HA displayed an improved intracellular uptake efficiency and enhanced tumor-targeted delivery. Thus, it provides better therapeutic action of NPs.^{9,40} TEM analysis of MDA-MB-231 cells displayed and confirmed that sufficient amounts of HA-PANi/R837 NPs were internalized by the target cells *via* the endocytic uptake mechanism and well observed in cytoplasmic distribution. Moreover, the cellular uptake of NP-treated cells was much higher and also coincided with the results of TEM analysis (Figure S6). Therefore, the cellular endocytic uptake of NPs was highly significant in specific targeted cells at all time points, clearly signifying that specific cellular uptake and internalization of NPs were strengthened due to the NP tumor-targeted molecule recognition on CD44-overexpressed TNBC cell receptors.^{42,46} These findings not only showed the functions of HA and its successful conjugation onto the NP

surface to enhance the specific cellular uptake but also confirmed the active targeting role of NPs *via* tumor cells' overexpressed CD44 receptors for enhanced uptake of therapeutic NPs. Afterward, NP endocytosis, the intracellular localization and distribution of NP-incubated cells, was directly visualized by cellular TEM imaging. Further, analysis of the cells treated with NPs observed under TEM images showed the locally cytoplasmic distribution of NPs in the form of aggregations. Then, HA was easily degraded into tiny fragments due to the presence of high-level hyaluronidase (Hyal) enzymes present in various tumors. Hyal-1 type is a major enzyme found in tumor tissues. Once HA binds with CD44 receptors on the tumor cell surface, it is cleaved into 50 saccharide long units by Hyal-2, forming caveolae. These caveolae develop endosomes and finally fuses with lysosomes. Then, the HA fragments are further degraded into tetrasaccharides by Hyal-1. This type of unique molecular-based degradation pathway is used for selective delivery into intracellular compartments. Thus, it is highlighted that the HA-based NPs can be potentially used for the targeted delivery of therapeutic molecules.^{38,39,42} The internalized NPs further exhibited a typical performance of aggregation in intracellular lysosomes, which could be accountable for their superior cancer photothermal therapeutic outcome. Therefore, according to our previous findings, PANi NP treatment could lead to rapid necrotic cell death upon NIR illumination due to the high cytotoxic photothermal activity.²⁸ Thus, we have concluded that HA-PANi/R837 NPs enhanced the specific intracellular uptake efficiency and delivered tumor-targeted PTA, which in turn makes them appropriate for PTCT strategy.

3.4. Selective Biocompatibility of NP-Treated Cells.

Furthermore, to explore the potential biomedical applications of nanomaterials, first, we need to test their potential biocompatibility and their associated toxicity on normal and tumor cells. For photothermal application of nanomaterials, they must be nontoxic in nature and highly biocompatible, which is a primary concern before applying NIR light illumination to activate the photothermal effect. In this study, we also assessed the *in vitro* cell compatibility using NIR light with different (0.5, 1.0, 1.5, and 2.0 W/cm²) power densities to evaluate the cytocompatibility. As shown in Figure 2a, the MDA-MB-231 tumor cells illuminated at four different power densities did not show any signs of toxicity toward the cell viability reduction even at a high power density of 2.0 W/cm² of the NIR light. Therefore, the NIR light used in this study exhibited excellent biocompatibility with the tested tumor cells unless the NIR light was combined with NPs. However, the biocompatible properties of nanomaterials are also tested using the typical methyl thiazolyl tetrazolium (MTT) assay on MDA-MB-231 tumor cells and non-tumorigenic MCF-10A normal human breast mammary epithelial cells that were treated with NPs and incubated for 24 h with various concentrations. Notably, in this study, we verified that even after 24 h of incubation there was no significant cell cytotoxic effect of NPs at different concentrations from 0.25 to 1.0 mg/mL. However, a very negligible amount of decreased cell viability was detected compared to the untreated control after the NPs were incubated with quite a high concentration of 1.0 mg/mL (Figure 2b). In detail, the dark cytotoxicity of NPs was evaluated at different concentrations from 0.1 to 1.0 mg/mL. The results exhibited very low toxicity and good biocompatibility of the NPs. Cell viability is

measured without irradiation on different concentration levels of NPs, namely, 0.25, 0.50, 0.75, and 1.0 mg/mL. At 0.25 mg/mL concentration of both NPs incubated with tumor cells, the cell viability was observed to be 99%, and at 0.50 mg/mL concentration, it resulted in nearly the same levels of 97 and 98%. It was further increased at the concentration of 0.75 mg/mL, and the cell viability level reached up to 95 and 96%. Therefore, more than 95% viability is demonstrated, which confirmed the highly significant biocompatibility of NPs. This well-known fact of enhanced biocompatibility is purely due to water-soluble HA moieties. Cells were still more viable and maintained, whereas after NP incubation, they showed only 85 and 90% at a concentration level of 1.0 mg/mL. Therefore, a high concentration decreased cell viability negligibly. These results demonstrated that the highest selective biocompatibility of NPs was observed in the treated MDA-MB-231 cells. Therefore, the biocompatibility results perfectly agree with the previously well-known reports.⁴⁶ The same trend was observed in the MCF-10A cells after treatment (Figure S7). The results demonstrated that NPs showed a nontoxic nature and insignificant cytotoxicity, thereby exhibiting the determination of biocompatible concentrations for further selectivity of effective photothermal tumor cell-killing agents.

3.5. *In Vitro* Intracellular ROS-Inducing Test of NPs.

The photothermal NPs in the cells should be highly biocompatible prior to investigating the NIR-light-induced PTCT, which also depends on the generation of intracellular reactive oxygen species (ROS)-related toxicity. Therefore, to assess the intracellular ROS level produced by NPs, using a ROS probe DCFH-DA is an effective approach to identify the ROS formed in biological systems. According to our previous report, PANi-poly(vinylpyrrolidone) (PVP) composite materials did not produce any significant levels of intracellular ROS even at the highest concentration, which showed high-level biocompatibility and effective PTCT under NIR light.²⁸ 2,7-Dichlorofluorescein diacetate (DCF-DA) is a universally used indicator of intracellular ROS production since it is non-fluorescent and could be oxidized into fluorescent DCF (green) in the presence of ROS. The diacetate DCFH (DCFH-DA) is cell-permeable that allows for ester loading of the dye, resulting in intracellular accumulation of non-fluorescent DCFH. Therefore, the green fluorescence property of DCF in NP-treated TNBC tumor cells was used to investigate intracellular ROS production. The present investigation demonstrated that almost no DCF fluorescence was observed in the untreated control group. Thus, we attempted to investigate whether the NPs can stimulate ROS generation in MDA-MB-231 cells; then, fluorescent green signals from DCF were observed under a fluorescent microscope after 24 h of NP treatment (Figure S8). We noticed that when the TNBC tumor cells were treated with NPs and incubated with the highest 0.50 mg/mL concentration, the intracellular ROS level was still negligible in the cells and trace green fluorescence was observed.⁴⁶ Hence, this ROS testing result green evidenced that NPs have very good biocompatibility and did not produce significant levels of intracellular ROS in the cells. These concentrations could be safe and biocompatible for further photothermal ablation of tumor cells.

3.6. Specific Receptor-Mediated *In Vitro* Photothermal Ablation. Encouraged by the high NIR light absorption capability, excellent PCE, and biocompatible properties of NPs, we were motivated to conduct further evaluations under a localized photothermal effect, and a

specific receptor-mediated photothermal ablation was demonstrated by the *in vitro* study. In this *in vitro* photothermal experiment, we used an 808 nm laser to provide the strongest evidence for the potent utilization of NPs as a NIR-1 therapeutic agent.^{31,50} As a proof of concept, the MTT assay was performed to study the targeted *in vitro* photothermal efficiency of NPs that showed different cell viability ranges in the tested MDA-MB-231 tumor cells. The highly biocompatible concentration of NPs used in this study is 0.50 mg/mL, which is due to the nontoxic nature that does not reduce cell viability. The untreated control cell viability was maintained at 100%. However, the NIR light illumination on MDA-MB-231 tumor cells also showed a cell viability of 98%. In a subsequent study, we also tested the MDA-MB-231 cells treated with NPs at 0.50 mg/mL, and the cell viability range reached maximum biocompatibility of about 99%. Furthermore, the MDA-MB-231 cells were treated with NPs under 808 nm NIR illumination ($\lambda_{\text{ex}} = 808 \text{ nm}$) and power density ($p = 1 \text{ W/cm}^2$) for 5 min ($t = 5 \text{ min}$). Thus, the clinical fact is that 1 W/cm² laser power and 5 min time were preferred to avoid normal cell damage. Therefore, complete tumor cell photothermal eradication was observed due to the active targeting effect of HA-PANi/R837 NPs on MDA-MB-231 tumor cells after NIR light illumination. This high percentage of MDA-MB-231 cancer cell death further elucidates the efficacy of NPs as the targeted photothermal therapeutic agent. Notably, the highest level of cellular uptake of NPs is observed that can be rationalized in terms of the increased receptor-mediated uptake by MDA-MB-231 tumor cells. Moreover, the specific targeted photothermal efficacy of nanomaterials was also assessed. Interestingly, a promising and substantial phototherapeutic response was observed, and a complete 100% photothermal tumor cell death after HA-PANi/R837 NPs with NIR light illumination proved a successful CD44-mediated targeted tumor cell photothermal action (Figure 2c). Throughout the NIR light illumination, the maximum absorbed NIR light was converted into heat energy to react and incinerate the MDA-MB-231 tumor cells, which is mainly responsible for photothermal ablation destroying the tumor cells. Thus, the maximum tumor cell ablation has been realized in the case of NP-targeted TNBC tumor cells as compared with the untreated control cells due to the substantial amount of light illumination that is validated with the percentage of cell viability. Additionally, we have also investigated the possible mechanism of NP-induced damage of the cell membrane *via* the experimental levels measured and noted the releases of lactate dehydrogenase (LDH) enzyme activity. LDH is a common marker used to study cell membrane damaging from selected cell types. The results authentically proved that the released percentages of the LDH level from the MDA-MB-231 cells incubated with various NP concentrations were obviously normal when compared to the untreated control cells, which suggested that no more observable cell membrane damage occurred or was induced by NPs alone (Figure S9).

3.7. Fluorescence Staining of Tumor Cells Induced by NPs. Furthermore, a dual staining experiment was carried out using calcein acetoxymethylester (calcein-AM) stain; green fluorescence to live cells and red fluorescence to dead cells were provided by propidium iodide (PI). This staining method was mainly used to distinguish the viable and dead cell stages. Under NIR illumination, NP-treated tumor cells were distinctly differentiated from green (for live viable cells) and red (for completely ablated cells), which was observed using

fluorescence microscopy. Subsequently, calcein-AM penetrated into the normal cell membrane, and the live cells displayed green fluorescence, whereas apoptotic/necrotic dead cells displayed red fluorescence due to their loss of membrane integrity and penetration of PI into the cells. Thus, CD44-overexpressed MDA-MB-231 cells treated with HA-PANi/R837 NPs under laser illumination displayed very clear red fluorescence, indicating that tumor cells were completely eradicated after photothermal treatment. MDA-MB-231 tumor cells treated with 0.50 mg/mL NPs are depicted in Figure 2d to distinguish the NP-dependent selective photothermal effect. As a proof-of-concept experiment, MDA-MB-231 tumor cells were treated at the concentration of 0.50 mg/mL and then NIR illuminated for 5 min and the cells exhibited tumor ablation. The completely ablated cells were observed to be reddish. While at the concentration of 0.50 mg/mL, NP alone treated cells without NIR were observed to be greenish, indicating viable cells and confirming great biocompatibility. It is well understood that the concentration of NPs leads to a high photothermal effect. This in turn induced more ablated dead cells, which were observed as red under NIR illumination. Therefore, most importantly, HA has high efficiency and specific binding affinity to CD44 receptor-overexpressed MDA-MB-231 tumor cells. They could be specifically recognized and can enter *via* a specific receptor-mediated targeted endocytosis pathway.⁴⁶

Subsequently, 808 nm NIR illumination activated the NPs to completely ablate CD44-overexpressed MDA-MB-231 tumor cells in a specific treatment area and showed a promising active targeted photothermal destruction effect. It has a striking specificity to destroy tumor cells, whereas no damages were observed without NIR illumination, and it does not affect the normal cells. According to the fluorescent images, the high level of specific cellular accumulation of NPs is extremely beneficial to efficiently ablate tumor cells. Notably, the hyperthermic effect of tumor cell ablation was very clearly observed in the designated region after PTCT caused by the antitumor effect of NPs. After all, the as-prepared NPs might be successfully doped using a biological dopant such as HA, and they exhibited strong NIR absorption. Thus, the ES form of PANi NPs was formed with high potency to ablate tumor cells by an effective targeted photothermal efficiency. Furthermore, the specific photothermal contribution of NPs during the apoptotic/necrotic stages was examined by the apoptotic quantification method. Thereafter, considering the high level of PCE, the highly efficient *in vitro* photothermal potential and excellent biocompatibility of NPs encouraged us to further carry out an *in vivo* animal experiment for this promising NP-based PTA for cancer treatment.

3.8. Flow Cytometric Quantification of Tumor Cell Ablation Induced by NPs. The apoptotic/necrotic stages of photothermal heat-ablated cells were quantified by flow cytometric analysis. A specific targeting performance of the NPs is an essential part of targeted anticancer therapy. Therefore, we wanted to quantitatively investigate the ablated MDA-MB-231 tumor cells. Highly effective photothermal material NP combinations were tested under NIR illumination at the cellular level to examine the quantification of apoptotic/necrotic cells. Thus, we conducted fluorescence-activated cell sorting (FACS), the data of which revealed a specific NP-dependent selective cellular uptake of the NPs in MDA-MB-231 cells. Necrosis and apoptosis are major cell death conditions that depend on the morphological changes of the

cells.²⁴ A typical pattern for apoptosis, PI-staining of cells, confirmed the DNA damage under NIR excited NPs. However, annexin/PI-staining established that a momentous proportion of treated cells displayed phosphatidylserine on the external side of an intact cell membrane disruption at least partly reflected the induction of genuine apoptosis cell death, relatively late apoptosis or secondary post-apoptotic necrosis, as the apoptosis (annexin⁺/PI⁻) cells have been readily observable at earlier time points. To evaluate whether the system induced a specific rate of apoptosis by targeted NP-treated MDA-MB-231 cells, they were assessed by quantifying the cellular uptake of PI after treatment with NPs for 24 h at a concentration of 0.50 mg/mL. In general, PI is impermeable to live cells, and the uptake of PI is used to quantify the apoptotic cell populations in which membrane integrity is lost. Quantification of apoptosis was performed, as shown in Figure 2e; the cells in the upper left-hand side represent the necrosis cell stage and the upper right-hand side, the late apoptotic cell stage, whereas those in the bottom left-hand side represent the viable live cell stage and the bottom right-hand side, the early apoptotic cell stage.

Amusingly, specific CD44 receptor-mediated endocytic uptake of NP-treated MDA-MB-231 cells took up PI in a comparison with the untreated control cells. There was increasing PI uptake with respect to 0.50 mg/mL concentration of NPs. Qualitative changes in the significant number of necrotic cells were observed after NPs were illuminated with NIR light. Using the highest biocompatible concentration had an advantage; 0.50 mg/mL dose after 24 h of incubation of NP formulations exhibited distinct necrotic performance due to the smaller size, and lysosomal aggregation showed the highest percentage. In Figure 2e, the control group of untreated MDA-MB-231 cells showed that there is no observable amount of apoptotic cells, as well as necrotic cell activities (0.03%) comparable with the live cell quantity (99.97%). However, at the same time, percentages of early and late apoptotic cells were also insignificant in the case of cells treated with NPs alone (0.05 and 0.02%) and necrotic cells (0.03%) and live cells (99.90%), which confirms that our NPs were highly biocompatible with the cells, and no significant apoptotic activity was noticed without NIR light. Meanwhile, the cells illuminated with NIR light alone showed the highest amount of live cells (94.48%) compared to the early apoptotic cells (0.15%), late apoptotic cells (0.03%), and necrotic cells (4.86%). More importantly, cells treated with NP formulations combined with NIR light illumination caused a highly significant increase in photothermal heat-ablated cell death that has the highest rate of the necrotic stage of cells observed (95.67%), compared with no early apoptotic cells and a negligible amount of late apoptotic cells (0.73%) (Figure S10). Thus, the results suggested that with the help of NIR light-activated NPs, enhanced photothermal heat-targeted necrotic ablation of tumor cells after CD44-mediated specific receptor-assisted internalization of NPs was observed. Therefore, the successful targeted delivery of NPs enhanced specific activation of the photothermal effect on targeted MDA-MB-231 cells, resulting in a highly therapeutic effect. Consequently, it could be ameliorated after treatment with HA-PANi/R837 NPs plus NIR light illumination. The maximum signals observed inside the MDA-MB-231 targeted cells were approximately 20-fold greater than the untreated control group. Therefore, such plentiful specific cellular uptake of the NPs could be attributed to the HA-cloaked PANi, wherein CD44 with the

homotypic ability of tumor self-recognition was present. To verify the homotypic targeting role of NPs, they were exposed to MDA-MB-231 cells and the untreated control cells to comparatively investigate their apoptotic prompting behaviors.⁴⁷ In contrast, higher levels of NPs were observed inside MDA-MB-231 cells, which specifies a highly homotypic satisfactory affinity. As stated above, the selected tumor cell membrane presented noticeable advantages of higher CD44 homologous distribution and targeting specific affinity with NPs.

3.9. Photothermally Induced ICD of NPs in Tumor Mice. Before investigating the photothermally induced ICD, we wanted to demonstrate the *in vivo* pharmacokinetic study of NPs. As shown in Figure S13, the NPs had a relatively long blood half-life of 3.1 h, possibly due to their nanosize, which could be effectively facilitated by the avoidance of clearance from the liver, kidney, and spleen. Furthermore, surface capping of HA enables the NPs to reduce rapid phagocytosis by macrophages. Furthermore, NIR-light-responsive NPs are widely used in PTCT for the ablation of tumor cells, and they are insufficient for inhibiting tumor metastasis and relapse at the present stage. Hence, we are trying to develop a novel system of an immunogenic combination to target the tumor site for combinatorial photothermal immunotherapy. In addition, antibodies are checkpoint blockades and were first developed for immunotherapy. Numerous CTLA-4 antibodies, including asipilimumab, nivolumab, pembrolizumab, atezolizumab, and ipilimumab, and programmed death-ligand 1 (PD-L1) have been approved by the FDA for advanced tumors.⁴⁴ However, several disadvantages associated with the antibodies are high cost, low stability, and potential immunogenicity. Therefore, low-weight molecular inhibitor checkpoints have been utilized for immunotherapy and are reported by several inhibitors.¹² Generally, it has been reported that many methods of tumor cell ablation treatments, such as PTCT, PDT, and radiotherapy, can help in inducing specific tumor immune responses by producing tumor-associated antigens. Therefore, it is contentious whether PTCT destroys the primary tumors and prevents metastasis when combined with R837 molecules, which act as an immune adjuvant. It could also induce effective antitumor immune responses in animal models. However, pristine R837 can promote DC maturation, due to low water solubility, which greatly restricts its use in clinical applications. Therefore, to overcome these limitations, R837 is loaded with carrier NPs.

As a novel composite, formation of HA layered onto the PANi nanocore facilitates the co-loading of hydrophobic R837 molecules for further immune stimulation. Previously, chlorin e6 (Ce6)-conjugated HA@aPD-L1, a three-in-one nanoplat-form, was demonstrated to be an excellent photothermal immunotherapeutic strategy against tumor metastases and relapses.⁵² By loading R837 with NPs, synergistic dual-model photothermal immunotherapeutic effects could be achieved. Under 808 nm NIR illumination, the NPs induced photothermal heat and immune activation by R837, which could effectively kill tumor cells. Meanwhile, the photothermal heat promotes R837 release and uptake by cells, which can further inhibit the growth of the tumor. Compared with traditional therapeutic strategies, the use of HA-PANi/R837 NPs is highly expected to be a more effective treatment for synergistic TNBC therapy. A well-established release of R837 was known to be at acidic pH, which is highly beneficial for binding with TLR7 within the tumor acidic endosomal compartment of the

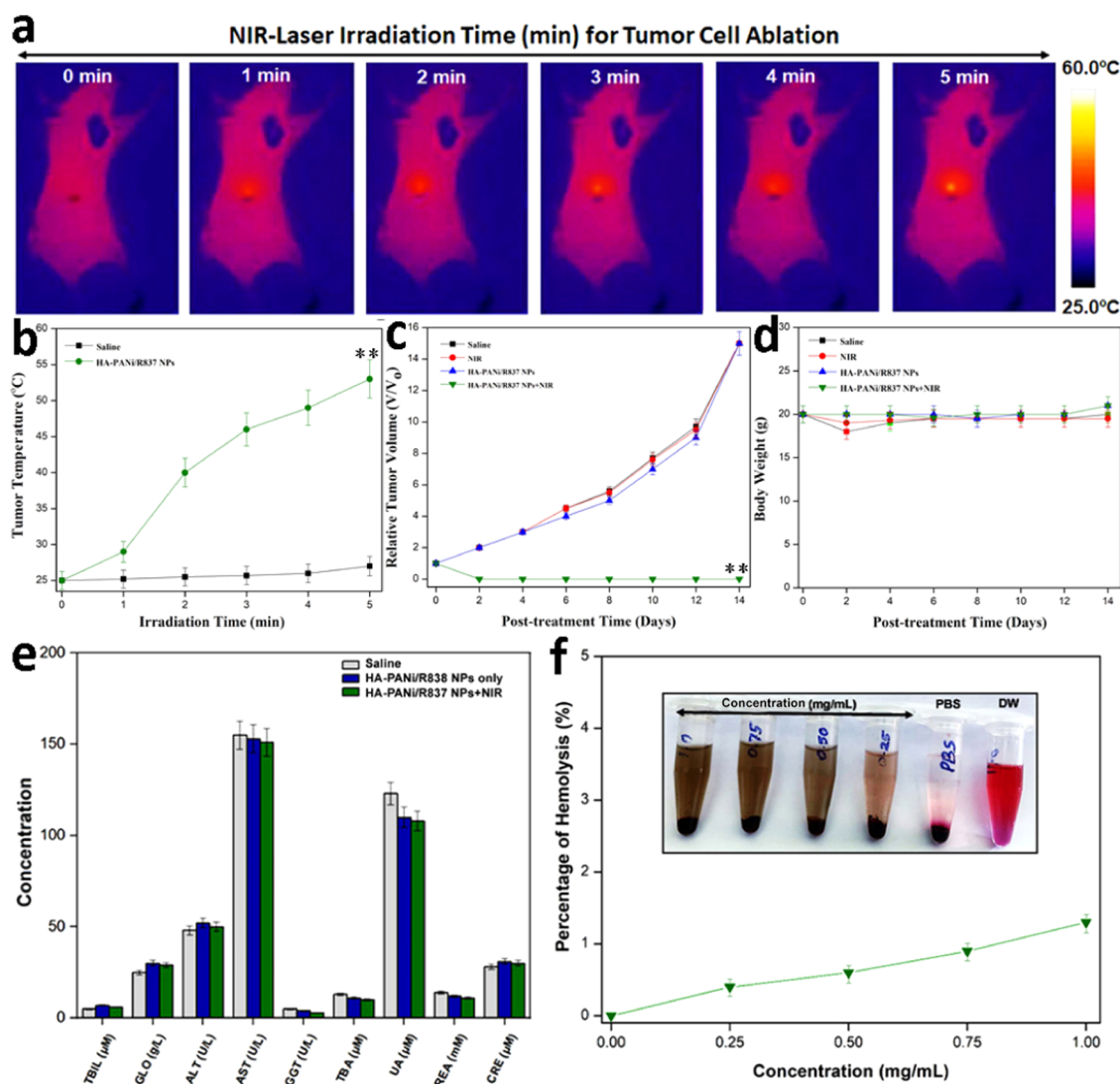


Figure 3. *In vivo* photothermal effect against the tumor. (a) Representative IR thermal photos of tumors in mice after various treatments with HA-PANI/R837 injection exposed to the NIR laser at the power density of 1 W/cm^2 recorded at different time intervals. As the control, IR thermal images of mice without NPs and saline injection exposed to the NIR laser at the power density of 1 W/cm^2 were taken. (b) Temperature progression profile on tumor-bearing mice during 5 min NIR illumination and injection with saline and HA-PANI/R837 NPs under the laser power of 1 W/cm^2 . The results are presented as means \pm SD. (c) Tumor growth rate curves of different groups of mice after treatment with and without NIR illumination. The tumor volumes were normalized to their initial sizes. Laser wavelength = 808 nm, power density = 1 W/cm^2 , and illumination time = 5 min. Error bars were based on standard deviations of five to seven mice per group. (d) Body weight of tumor-bearing mice of different groups during the treatment period. Data are shown as the mean \pm SD. Statistically significant values, **compared with the control group, $P < 0.01$. (e) Blood biochemical analysis data of mice 15 days after HA-PANI/R837 NPs and HA-PANI/R837 NP-based photothermal treatment (1 W/cm^2). Age-matched healthy mice were used as the control group. Levels of TBIL, GLO, ALT, AST, GGT, TBA, UA, UREA, and CRE from the healthy control and treated mice. The complete blood panel data from the healthy control and treated mice. All of the parameters of the blood analysis fell well within the normal range. No significant difference in all blood test data was noticed between the control and the treated groups. Error bars were based on five mice per group. (f) Percentage hemolysis ratio corresponding to the photograph (inset) of the NPs in various media, including water, PBS, and PBS containing different NP concentrations (0.25, 0.50, 0.75, and 1 mg/mL).

target cell. The accelerated R837 release in response to low pH may be a result of protonation of R837 aromatic amines in acidic conditions. We therefore assumed that HA was enzymatically degraded by excess Hyal-1 present in the tumor microenvironment into small HA fragments, while R837 was simultaneously released because of the decreased electrostatic interaction (Figure S11). Apart from the acidic pH tumor microenvironment condition, we have also tested the percentage release of R837 from NPs under 808 nm NIR light illumination. The results very clearly demonstrated that the R837 percentage release also depends on NIR illumination

(Figure S12). The released R837 percentage was evaluated under NIR illumination with various power densities for 5 min. The results confirmed that the optimum power density of 1 W/cm^2 could be used for further R837 release experiments. Previous reports demonstrated that Fe_3O_4 -R837 NPs have successfully been utilized for photothermal cancer immunotherapy.⁵³

Therefore, cancer immunotherapy is commonly used to recognize and destroy the tumor cells engaged with the patients' own immune system than the exogenous toxicants. Thus, immunotherapy is an attractive strategy in targeting

TNBC because of its high immune specificity and efficiency,¹² although the tumor can escape the checkpoints, which leads to immune tumor evasion or resistance. Therefore, immune checkpoints are to be considered as a novel tool in targeting tumor immunotherapy.⁴⁴ Furthermore, we have also investigated the activation of immune responses attributed to the activation of T cells, which is mainly responsible for directly killing the tumor-specific targeted TNBC cells. Dendritic cells (DCs) are antigen-presenting cells (APCs) activating native T cells. Immature DCs (iDCs) take up the surrounding tumor environment antigens and process them into peptides during migration for T cell activation. Therefore, we investigated the immune response of HA-PANi/R837 NPs; R837, a kind of toll-like receptor 7 (TLR7) agonist, could promote dendritic cell maturation (mDC), phagocytize the tumor-associated antigens, and become mature. Accordingly, it also enhances the activation and proliferation of antigen-specific lymphocytes in draining lymph nodes (DLNs). Moreover, DCs are a type of antigen-presenting cells (APCs), which can mature by capturing antigens to activate T cells.

Encouraged by the aforementioned results of active NP-induced targeted photothermal ablation of MDA-MB-231 tumor cells *in vitro*, we then investigated the *in vivo* targeted photothermal tumor efficacy using NPs to enhance the photothermal immunotherapeutic agent in a tumor mice animal model. Consequently, ES PANi NPs are well-suitable as an excellent photothermal therapeutic agent under 808 nm NIR illumination, and they do not affect the blood or normal tissue.²⁸

In our tumor animal model experimental study, we have demonstrated the tumor photothermal *in vivo* heat response, photostability, and photothermal treatment that triggered the incineration of the tumor with efficient growth inhibition of tumor by targeted NPs. To observe efficient *in vivo* photothermal effects, thermographic tumor infrared maps and the tumor temperature changes were recorded simultaneously using an infrared thermal imaging camera. The tumor mice were randomly divided into four groups ($n = 5$ per group), and experimental treatments were performed using the following conditions: (1) control saline group, (2) treatment group of only 808 nm NIR illumination, (3) treatment group of NPs without 808 nm NIR exposure (HA-PANi/R837 NPs), and (4) treatment group of HA-PANi/R837 NPs exposed to 808 nm NIR (HA-PANi/R837 NPs + NIR laser). Treatment groups of tumor mice were intratumorally administered a combination of HA-PANi/R837 NPs (0.5 mg/mL, 100 μ L), followed by 808 nm NIR illumination for 5 min with a power density of 1 W/cm². A gradual increase in temperature was observed from the IR thermal images (Figure 3a).

Furthermore, as displayed in Figure 3b, we have also recorded the tumor temperature profile measurement of NPs observed using a thermal imager under 808 nm NIR illumination. In the control saline group, there is no significant increase in the tumor temperature of the mice group, which confirms that there is no tumor ablation. At the same time, upon NIR illumination of light energy at the target tumor site, the PCE of NPs was increased, which could substantially increase the tumor temperature for photothermal ablation of the tumor mass. Thus, with the assistance of the homologous targeting property of our NPs, we achieved temperatures of above 50 °C within 5 min of NIR illumination. Such an excellent property of high significance in organic polymer-based PTCT was effectively developed, and increased tumor

temperature cooperatively provided a way for successive antitumor therapy.^{22,25,49} In addition, the control group of the untreated tumor mice was not administered NPs without NIR laser illumination. Moreover, the actual tumor size was measured once in 2 days using a digital electronic caliper.

Every day the change in tumor volume after the different treatments in all of the groups was monitored. We found that the size of the tumor in the control group, the NIR laser alone, and the NPs alone groups gradually increased, whereas, at the same time, the tumor growth in HA-PANi/R837 NP-treated groups was inhibited, suggesting that PTCT contributed to tumor cell ablation. Therefore, at the end of the 14th day of the *in vivo* animal experiment, the relative tumor volume of mice treated with NPs was compared with those of other groups under 808 nm NIR laser illumination and displayed a highly significant reduction in tumor volume (Figure 3c). Expectedly, the NPs with laser illumination group exhibited highly significant tumor eradication. Notably, the NPs had specific tumor growth reduction and better efficiency, which in turn showed complete tumor disappearance. This could be due to the CD44-mediated specific tumor cell uptake of NPs. These *in vivo* results suggested that a suitable level of hyperthermic effect could enhance the NPs after entering into the tumor tissue and subsequently improve intratumoral accumulation, which might enable further eradication leading to the high efficiency of the PTCT treatment. More importantly, the NPs showed nontoxicity and good biocompatibility since changes in body weight were scarcely found (Figure 3d). Therefore, these findings of the present study confirmed that HA-PANi/R837 NPs have great potential for *in vivo* tumor treatment. In an earlier report, successful designing of a new combination of PLGA-ICG-R837-based NPs for effective photothermal immunotherapy *in vitro* and *in vivo* was achieved.⁵⁴ As a result, the combination of HA-PANi/R837 with desirable NIR therapy at the exact tumor site resulted in the high performance of tumor eradication, which was confirmed using TNBC models.

Additionally, we have also examined the well-known serum biochemistry levels quantitatively, which are mainly used to assess the toxicological effect of the administrated NPs.⁵⁵ Thus, the six major hepatic important indicators of normal healthy liver functions are TBIL, GLO, ALT, AST, GGT, and TBA, and the other four main indicators of normal healthy kidney functions, such as GGT, UA, UREA, and CRE, were measured. Expectedly, all of these major biochemical indicators of liver and kidney function levels did not show any significant changes during NP administration, similar to the untreated control group (Figure 3e). Consequently, these above-stated results proposed that NPs exhibited nontoxicity in living systems. However, more efforts to study the long-term effects of NPs are still required.

Subsequently, it is also a prime concern to evaluate the blood biocompatibility of our NPs prior to the *in vivo* animal experiment, which is expected to possess a good hemocompatible property. Thus, the hemocompatibility and the nontoxicity property of NP blood components were estimated using the American Society for Testing and Materials (ASTM) hemolysis standard assay.²⁴ The quantitative values based on the supernatant absorbance at 541 nm were calculated (Figure 3f). Thus, the percentage ratio of hemolysis is less than 2% at the maximum tested experimental concentration (1 mg/mL), which confirmed that the NPs have good hemocompatibility lower than the pharmacopeia necessity of 5%. The results are

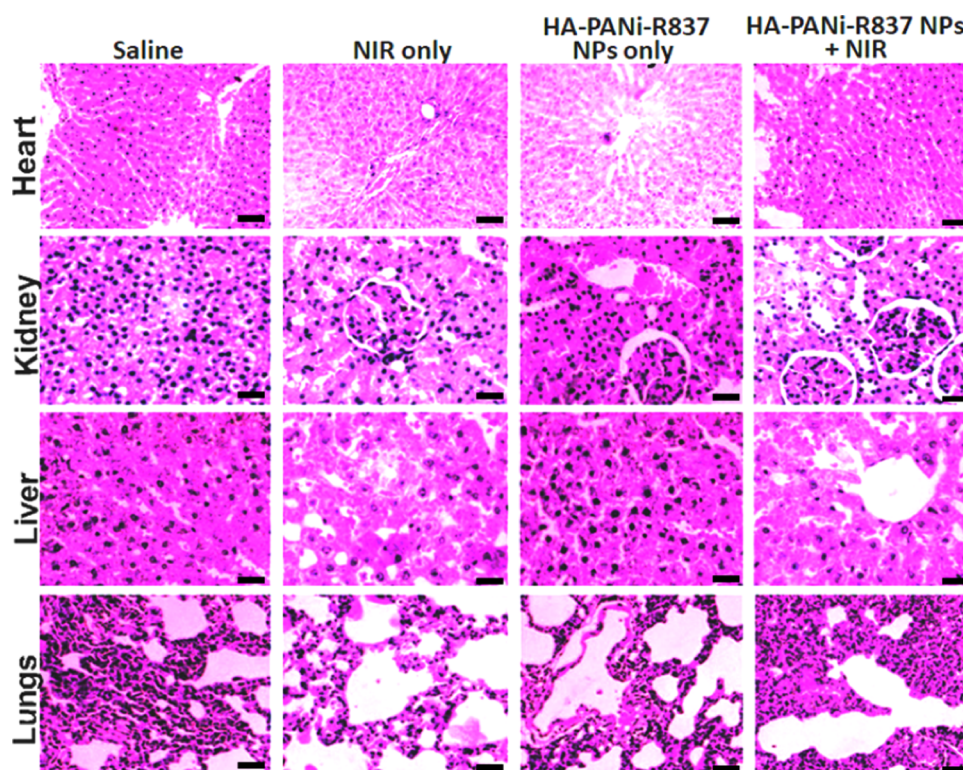


Figure 4. Histological examination of various organs after different treatments. Histological H&E-stained images of major organs such as heart, kidney, liver, and lungs of the tumor-bearing mice at the end of 14 days after various treatments. (The scale bar is 100 μm for all panels).

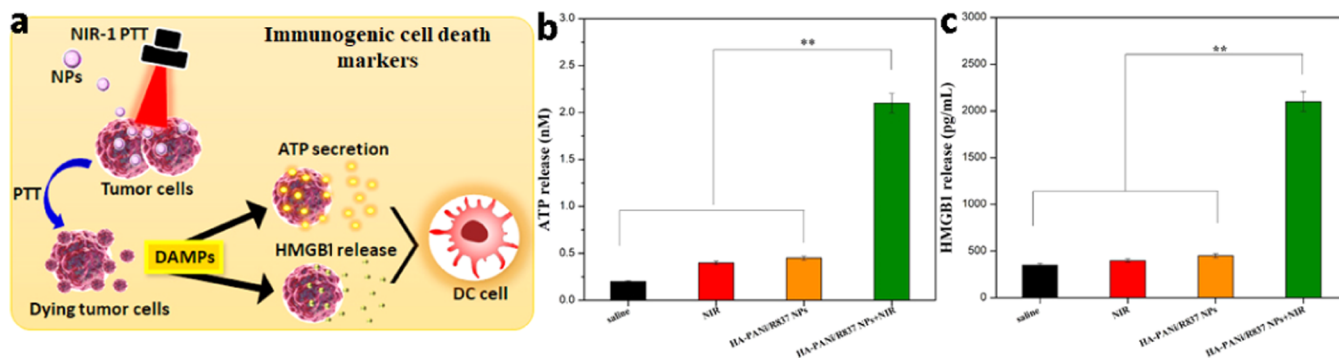


Figure 5. (a) Immunogenic cell death markers were measured after the tumor cell treatment with NPs undergoing ICD produced by DAMPs (b) ATP secretion and (c) HMGB1 release. All of the data are presented as the mean \pm standard error of the mean (s.e.m.). Error bars are based on triplicated experiments. Statistically significant values compared with the control group, P values: * $P < 0.05$ and ** $P < 0.01$.

similar to those of the previously reported PANi NPs for photothermal–photodynamic therapy (PTT) and PAI.³⁵ However, we obviously found the hemolysis of red blood cells in the positive water control, which suggests that the tested NPs have high hemocompatible property and could be suitable for *in vivo* administration in experimental animals for anticancer treatment. The results indicated that the highest hemocompatibility benefitted from inheriting HA biocompatibility and excellent water solubility.

Furthermore, to study the histology of tumor mice injected with NPs, major organs such as heart, kidney, liver, and lung were harvested at the end of the *in vivo* animal experiment. The mice without any administration of injection were used for comparison (untreated control group); thus, the H&E staining results revealed that there is no direct evidence of observable adverse effects affected by NPs (Figure 4). For further evaluation of the HA-PANi/R837 NP accumulation inside

the tumor and the tumor target effect, the PAI of TNBC tumors at various time points after the administration of these NPs could prove the tumor-targeting efficiency. Owing to the excellent NIR-light-responsive property of NPs, their potential photoacoustic contrast imaging agents were expected to monitor the accumulation of the NPs in the tumor site, which could provide guidance for therapy. Upon NIR light illumination on NPs, brighter and stronger PAI signals (Figure S14a) on increasing the concentration of NPs were generated. After administration of the NPs, PAI signals of the tumor site were recorded at different time points, shown in Figure S14b as PAI signal data obtained by quantitative analysis; PAI signals at the tumor site were progressively enhanced within 12 h and then decreased after 24 and 48 h. Therefore, this result demonstrated that the maximum tumor accumulation of these NPs was achieved approximately at 12 h of administration.

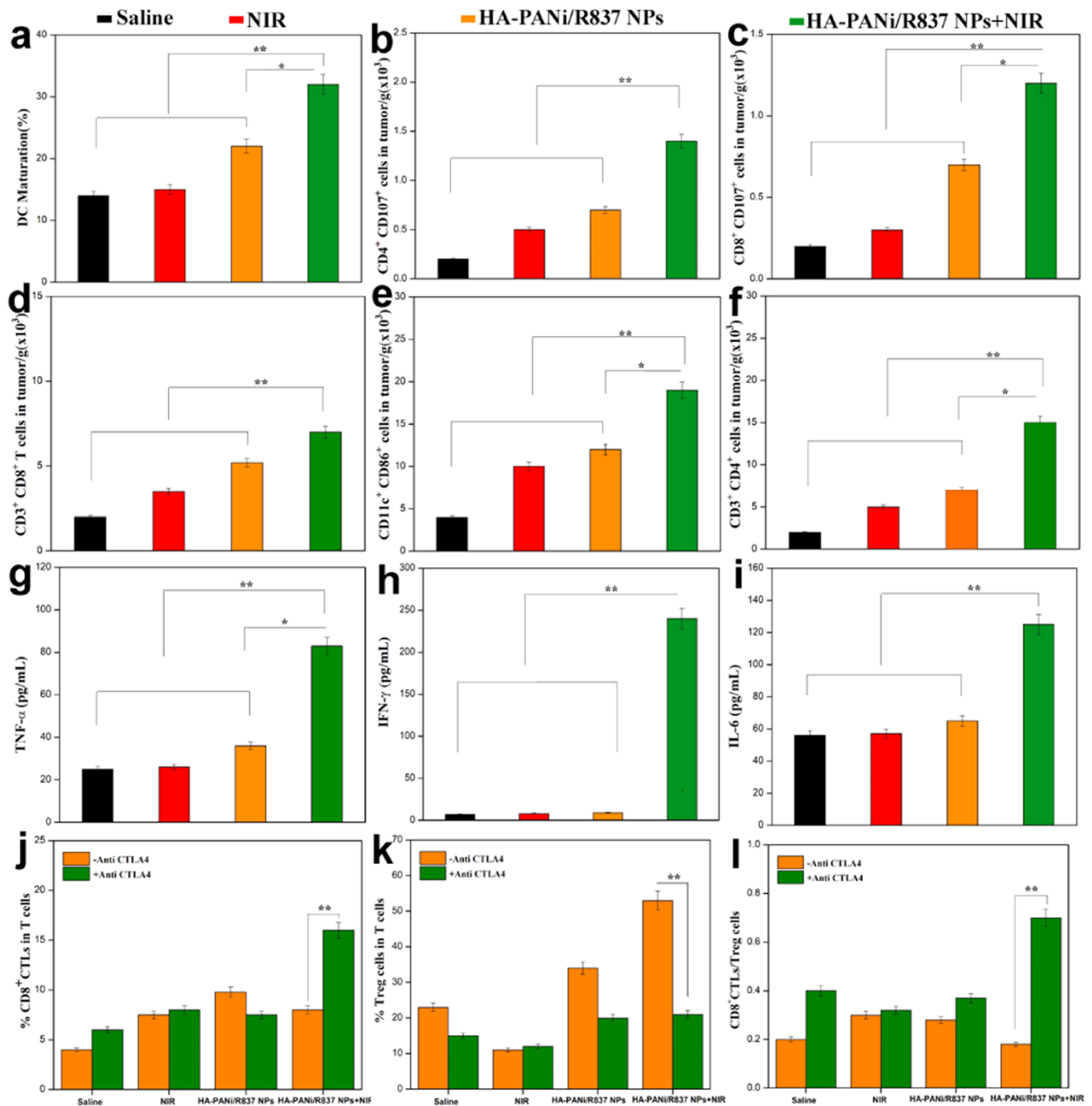
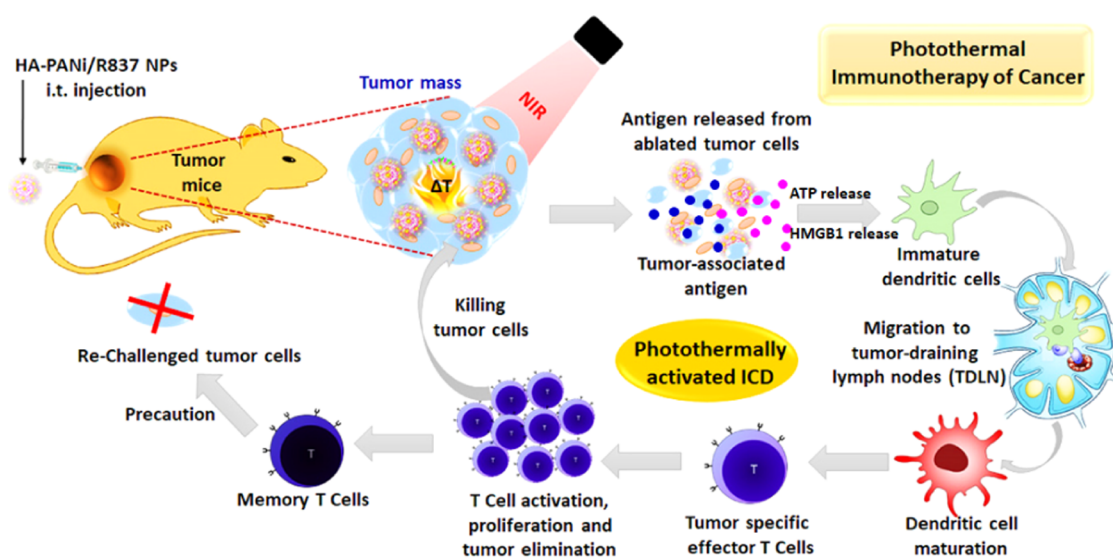


Figure 6. *In vivo* immunological effect against tumor. (a) NP-based immune-stimulation abilities in *in vivo* DC maturation with lymph nodes of mice injected with saline, NIR, HA-PANi/R837 NPs, and HA-PANi/R837 NPs + NIR (totally three mice per group). Infiltration of (b) CD11c⁺CD86⁺ DCs, (c) CD3⁺CD4⁺ T cells, (d) CD3⁺CD8⁺ T cells, (e) activated CD4⁺ T cells, and (f) activated CD8⁺ T cells in the tumor ($n = 3$). (g–i) Cytokine levels in the serum from tumor-bearing mice isolated after injection ($n = 3$). Antitumor immune effects and the related mechanisms of HA-PANi/R837-based PTT in combination with CTLA-4 checkpoint blockade. (j) Proportions of tumor-infiltrating CD8⁺ killer T cells and (k) CD4⁺FoxP3⁺ effector T cells (Treg) in the collected tumor (l) CD8⁺ CTL to Treg ratios in tumors for different groups of mice. All of the data are presented as the mean \pm s.e.m. Error bars are based on triplicated experiments. Statistically significant values compared with the control group, P values: * $P < 0.05$ and ** $P < 0.01$.

3.10. NP-Mediated, PTT-Induced, and ICD-Activated Antitumor Immune Response. Promisingly, advanced nanotechnology methods are able to enhance the efficacy of small immunostimulatory therapeutic drug molecules in altering their biodistribution. Therefore, immunostimulatory molecules were delivered using NPs to achieve antitumor immune cell activation, which was more efficient in eliminating

tumor cells than chemotherapeutics.^{45,56} Emerging evidence demonstrate that immunotherapies of tumors greatly improve the strong antitumor effects.⁵⁷ A well-known fact is that DCs are important originators of immune responses and are enormously significant targets for antitumor nanomedicines. Overall, adequate antitumor immunity should have effective stages, such as tumor-associated antigens can be released from

Scheme 2. Schematic Summarizing the Mechanisms of NIR-Mediated PTCT with CTLA-4 Checkpoint Blockade for Cancer Immunotherapy^a



^aHA-PANi/R837 NPs illuminated with NIR light enable effective photothermal destruction of tumors. The generated tumor-associated antigens in the presence of NPs as the adjuvant are able to promote strong antitumor immune responses with assistance of a CTLA-4 checkpoint blockade and can eliminate the primary tumors under direct NIR light exposure, inhibiting distant tumor growth left behind after PTCT, promoting a long-term immune cell memory to prevent tumor reoccurrence.

destroyed tumors after which they can be effectively taken up and managed in existing DCs. Subsequently, activation of DCs results in their migration to the tumor-draining lymph nodes for further promoting immune effector cells by stimulating cytokines. Furthermore, the ICD markers of damage-associated molecular patterns (DAMPs) in the extracellular region secreted ATP and HMGB1 release from tumor dying cells, which were measured using an ATP assay kit and an ELISA assay kit, respectively (Figure 5a–c). The extracellular ATP level and HMGB1 release levels in tumor cells treated with NPs did not significantly change in the absence of irradiation compared to the control group. However, both DAMPs (secreted levels of ATP and HMGB1 release level) were increased in tumor cells treated with NPs under irradiation compared with other treatment groups. The dying tumor cells generate DAMPs by PTT-induced ICD, which can activate antigen-presenting cells to stimulate the production of tumor-specific T cells.

The immune-related cytokines from DCs, including tumor necrosis factor α (TNF- α is a key marker for cellular immunity activation) and interleukin 6 (IL-6 is also a key marker of cellular immunity), are measured and considered to be indicators of DC activation. More interestingly, photothermal ablation of tumor in addition to immunoadjuvant HA-PANi NPs under laser illumination induced an increased level of mDC (>30%) (Figure 6a), which is found to be significantly higher than that of adjuvant R837 with HA-PANi NPs in the absence of NIR. Therefore, post-PTCT, the DCs also engaged to trigger immune responses.

The pivotal role of cytotoxic T lymphocytes (CTLs) ($CD3^+CD4^-CD8^+$) can kill targeted tumor cells directly. However, helper T cells ($CD3^+CD4^+CD8^-$) play an essential role in adaptive immunity regulation.⁵⁴ Therefore, in the present study experiments, the estimated level of CTL in the tumor mice after the HA-PANi/R837 NP-based PTCT treatment significantly increased, which was found to be

significantly higher compared to the saline, NIR, and NPs without NIR groups (Figure 6b–f). Finally, cytokine secretion *in vivo* is also known to be important for immune responses. In a similar experimental work, after the different treatments, the mice serum was collected to analyze several cytokines, such as TNF- α , IL-6, and IFN- γ . We found under NIR illumination, the NPs boosted the enhancement of TNF- α and IL-6 levels post-treatment with HA-PANi/R837 NPs (Figure 6g–i). Moreover, there is no appreciable difference in immune response enhancements in saline, NIR, and NP alone groups. Thus, cytokines of TNF- α and IFN- γ are major markers of cellular immunity, playing a role in the fight against cancer to enhance immunotherapeutic efficiency. The serum levels of both TNF- α and IFN- γ were significantly increased in the mice treated with HA-PANi/R837-based PTCT, particularly for the group with PTCT plus the second round of immune system activation, demonstrating successful antitumor immune response establishment. Additionally, no obvious enhancement was found in the saline untreated control.

Thus, the designed NPs could boost a strong immune response against tumor cells. Therefore, NPs had a durable efficacy in triggering DC maturation and antitumor immune activation. Thus, it is very clearly noticed that immunogenic responses triggered by NP-based photothermal destruction of the tumor combined with anti-CTLA-4 therapy could effectively inhibit cancer metastasis and prolong the survival of mice. Therefore, HA-PANi/R837 NP-dependent PTCT with anti-CTLA-4 induced a high-level percentage of $CD8^+$ CTLs and $CD8^+$ CTL/Treg, which are mainly responsible for cellular immunity in cancer immunotherapy (Figure 6j–l). Our data strongly evidenced that HA-PANi/R837 NP-based therapy could improve the activation of a strong immune effect based on ICD to effectively prevent the reoccurrence of tumors (Scheme 2).

4. CONCLUSIONS

In summary, we have successfully developed a combined system to understand the tumor-specific CD44 receptor-mediated targeting nanotherapeutics for the activation of photothermal ICD. This NP-based targeting immune system activation is highly promising for the development of innovative concepts that provide new insights into addressing TNBC treatment. Consequently, smart NPs exhibited a high molar extinction coefficient and PCE and demonstrated excellent PCTC under prominent NIR irradiation, which is highly beneficial for selective receptor-mediated photothermal ablation of TNBC cells. Therefore, the NPs with good biocompatibility are highly suitable, while co-encapsulation with R837 and clinically approved anti-CTLA-4 checkpoint blockade therapy promote a strong antitumor immune response against target TNBC tumor cells for the stimulation of ICD with a homotypic active tumor-targeting capacity of NPs at the tumor site. Therefore, we believe that this work has demonstrated promising potential for PTCT with immunotherapy to realize a synergistic therapeutic outcome in eliminating and preventing tumor relapse.

■ ASSOCIATED CONTENT

SI Supporting Information

The Supporting Information is available free of charge at <https://pubs.acs.org/doi/10.1021/acs.biomac.1c00244>.

Regression equation determined by the absorbance at 322 nm versus the feeding concentration of R837; encapsulation and loading efficiencies of R837; UV-vis spectrum of HA and R837 alone; HA-PANi/R837 NP dispersion with different concentrations and illuminated by 808 nm NIR light with different power densities; photostability of HA-PANi/R837 NP dispersion in PBS and DMEM, NPs compared with ICG under continuous laser illumination (808 nm, 1 W/cm²) with repeated five on/off cycles, and the normalized intensity change of free ICG and NPs in aqueous solution for different time points; TEM analysis of the intracellular uptake of NPs; MCF-10A cell viability of HA-PANi NP- and HA-PANi/R837 NP-treated normal cells with various concentrations of 0.25–1 mg/mL compared with the untreated control; intracellular ROS assay using DCFH-DA fluorescence staining; levels of released LDH from cells after being exposed to various concentrations of NPs; quantitative analysis of apoptotic cells by FACS; released percentage of R837 from HA-PANi NPs with and without NIR irradiation; released percentage of R837 from HA-PANi NPs with 808 nm NIR irradiation at different power densities for 5 min; pharmacokinetics profiles of NPs after injection into the mice; and PAI of the NPs at different concentrations in the range of 0.25–1.0 mg/mL and quantitative PAI signal values and PAI signals at different time points (PDF)

■ AUTHOR INFORMATION

Corresponding Author

Raju Vivek – Cancer Research Program (CPR), Bio-Nano Therapeutics Research Laboratory, Department of Zoology, School of Life Sciences, Bharathiar University, Coimbatore 641046, India; orcid.org/0000-0002-1860-908X; Email: vivekr@buc.edu.in

Authors

Vellingiri Yasothamani – Cancer Research Program (CPR), Bio-Nano Therapeutics Research Laboratory, Department of Zoology, School of Life Sciences, Bharathiar University, Coimbatore 641046, India

Laxmanan Karthikeyan – Cancer Research Program (CPR), Bio-Nano Therapeutics Research Laboratory, Department of Zoology, School of Life Sciences, Bharathiar University, Coimbatore 641046, India

Selvaraj Shyamsivappan – Department of Chemistry, School of Chemical Sciences, Bharathiar University, Coimbatore 641046, India

Yuvaraj Haldorai – Department of Nanoscience and Technology, Bharathiar University, Coimbatore 641046, India

Dayakar Seetha – Rajiv Gandhi Centre for Biotechnology, Thiruvananthapuram 695585, Kerala, India

Complete contact information is available at:

<https://pubs.acs.org/doi/10.1021/acs.biomac.1c00244>

Notes

The authors declare no competing financial interest.

■ ACKNOWLEDGMENTS

This research work is fully supported by the Department of Biotechnology, Ministry of Science and Technology, Government of India, to whom the authors are grateful for providing this project (D.O.NO.BT/HRD/35/02/2006 dt: 2018) and Bharathiar University for constant support.

■ REFERENCES

- (1) Siegel, R. L.; Miller, K. D.; Jemal, A. Cancer Statistics. *CA—Cancer J. Clin.* **2017**, *67*, 7–30 2017.
- (2) Cao, Y.; DePinho, R. A.; Ernst, M.; Vousden, K. Cancer research: past, present and future. *Nat. Rev. Cancer* **2011**, *11*, 749–754.
- (3) Weigelt, B.; Peterse, J. L.; van't Veer, L. J. Breast cancer metastasis: Markers and models. *Nat. Rev. Cancer* **2005**, *5*, 591–602.
- (4) Sledge, G. W.; Mamounas, E. P.; Hortobagyi, G. N.; Burstein, H. J.; Goodwin, P. J.; Wolff, A. C. Past, Present, and Future Challenges in Breast Cancer Treatment. *J. Clin. Oncol.* **2014**, *32*, 1979–1986.
- (5) Hayes, D. F. Further Progress for Patients with Breast Cancer. *N. Engl. J. Med.* **2019**, *380*, 676–677.
- (6) Sinn, H. P.; Kreipe, H. A Brief Overview of the WHO Classification of Breast Tumors, 4th Edition, Focusing on Issues and Updates from the 3rd Edition. *Breast Care* **2013**, *8*, 149–154.
- (7) de Bono, J. S.; Ashworth, A. Translating cancer research into targeted therapeutics. *Nature* **2010**, *467*, 543–549.
- (8) Workman, P.; de Bono, J. Targeted therapeutics for cancer treatment: major progress towards personalised molecular medicine. *Curr. Opin. Pharmacol.* **2008**, *8*, 359–362.
- (9) Al-Mahmood, S.; Sapiezynski, J.; Garbuzenko, O. B.; Minko, T. Metastatic and triple-negative breast cancer: challenges and treatment options. *Drug Delivery Transl. Res.* **2018**, *8*, 1483–1507.
- (10) Hudis, C. A.; Gianni, L. Triple-Negative Breast Cancer: An Unmet Medical Need. *Oncologist* **2011**, *16*, 1–11.
- (11) Guo, P.; Yang, J.; Liu, D. X.; Huang, L.; Fell, G.; Huang, J.; Moses, M. A.; Auguste, D. T. Dual complementary liposomes inhibit triple-negative breast tumor progression and metastasis. *Sci. Adv.* **2019**, *5*, No. eaav5010.
- (12) Marra, A.; Viale, G.; Curigliano, G. Recent advances in triple negative breast cancer: the immunotherapy era. *BMC Med.* **2019**, *17*, No. 90.
- (13) Le Du, F.; Ueno, N. T. Targeted therapies in triple-negative breast cancer: failure and future. *Women's Health* **2015**, *11*, 1–5.

- (14) Kutty, R. V.; Leong, D. T. W.; Feng, S.-S. Nanomedicine for the treatment of triple-negative breast cancer. *Nanomedicine* **2014**, *9*, 561–564.
- (15) Prabhakar, U.; Maeda, H.; Jain, R. K.; Sevick-Muraca, E. M.; Zamboni, W.; Farokhzad, O. C.; Barry, S. T.; Gabizon, A.; Grodzinski, P.; Blakey, D. C. Challenges and Key Considerations of the Enhanced Permeability and Retention Effect for Nanomedicine Drug Delivery in Oncology. *Cancer Res.* **2013**, *73*, 2412–2417.
- (16) Li, J. Nanotechnology-based platform for early diagnosis of cancer. *Sci. Bull.* **2015**, *60*, 488–490.
- (17) Chan, W. C. W.; Udugama, B.; Kadhiresan, P.; Kim, J.; Mubareka, S.; Weiss, P. S.; Park, W. J. Patients, Here Comes More Nanotechnology. *ACS Nano* **2016**, *10*, 8139–8142.
- (18) Tong, R.; Tang, L.; Ma, L.; Tu, C. L.; Baumgartner, R.; Cheng, J. J. Smart chemistry in polymeric nanomedicine. *Chem. Soc. Rev.* **2014**, *43*, 6982–7012.
- (19) Sharman, W. M.; van Lier, J. E.; Allen, C. M. Targeted photodynamic therapy via receptor mediated delivery systems. *Adv. Drug Delivery Rev.* **2004**, *56*, 53–76.
- (20) Priya James, H.; John, R.; Alex, A.; Anoop, K. R. Smart polymers for the controlled delivery of drugs - a concise overview. *Acta Pharm. Sin. B* **2014**, *4*, 120–127.
- (21) Kim, S.; Kim, J.-H.; Jeon, O.; Kwon, I. C.; Park, K. Engineered polymers for advanced drug delivery. *Eur. J. Pharm. Biopharm.* **2009**, *71*, 420–430.
- (22) Jung, H. S.; Verwilt, P.; Sharma, A.; Shin, J.; Sessler, J. L.; Kim, J. S. Organic molecule-based photothermal agents: an expanding photothermal therapy universe. *Chem. Soc. Rev.* **2018**, *47*, 2280–2297.
- (23) de Melo-Diogo, D.; Pais-Silva, C.; Dias, D. R.; Moreira, A. F.; Correia, I. J. Strategies to Improve Cancer Photothermal Therapy Mediated by Nanomaterials. *Adv. Healthcare Mater.* **2017**, *6*, No. 1700073.
- (24) Vivek, R.; Thangam, R.; Kumar, S. R.; Rejeeth, C.; Sivasubramanian, S.; Vincent, S.; Gopi, D.; Kannan, S. HER2 Targeted Breast Cancer Therapy with Switchable "Off/On" Multifunctional "Smart" Magnetic Polymer Core-Shell Nanocomposites. *ACS Appl. Mater. Interfaces* **2016**, *8*, 2262–2279.
- (25) Yang, J.; Choi, J.; Bang, D.; Kim, E.; Lim, E.-K.; Park, H.; Suh, J.-S.; Lee, K.; Yoo, K.-H.; Kim, E.-K.; Huh, Y.-M.; Haam, S. Convertible Organic Nanoparticles for Near-Infrared Photothermal Ablation of Cancer Cells. *Angew. Chem., Int. Ed.* **2011**, *50*, 441–444.
- (26) Qi, J.; Fang, Y.; Kwok, R. T. K.; Zhang, X. Y.; Hu, X. L.; Lam, J. W. Y.; Ding, D.; Tang, B. Z. Highly Stable Organic Small Molecular Nanoparticles as an Advanced and Biocompatible Phototheranostic Agent of Tumor in Living Mice. *ACS Nano* **2017**, *11*, 7177–7188.
- (27) Xu, L. G.; Cheng, L.; Wang, C.; Peng, R.; Liu, Z. Conjugated polymers for photothermal therapy of cancer. *Polym. Chem.* **2014**, *5*, 1573–1580.
- (28) Wang, L.; Vivek, R.; Wu, W.; Wang, G.; Wang, J.-Y. Fabrication of Stable and Well-Dispersed Polyaniline-Polypyrrolidone Nanocomposite for Effective Photothermal Therapy. *ACS Biomater. Sci. Eng.* **2018**, *4*, 1880–1890.
- (29) Li, J. C.; Pu, K. Y. Development of organic semiconducting materials for deep-tissue optical imaging, phototherapy and photoactivation. *Chem. Soc. Rev.* **2019**, *48*, 38–71.
- (30) Jain, P. K.; Huang, X. H.; El-Sayed, I. H.; El-Sayed, M. A. Noble Metals on the Nanoscale: Optical and Photothermal Properties and Some Applications in Imaging, Sensing, Biology, and Medicine. *Acc. Chem. Res.* **2008**, *41*, 1578–1586.
- (31) Zhou, J.; Lu, Z.; Zhu, X.; Wang, X.; Liao, Y.; Ma, Z.; Li, F. NIR photothermal therapy using polyaniline nanoparticles. *Biomaterials* **2013**, *34*, 9584–9592.
- (32) Yslas, E. I.; Ibarra, L. E.; Molina, M. A.; Rivarola, C.; Barbero, C. A.; Bertuzzi, M. L.; Rivarola, V. A. Polyaniline nanoparticles for near-infrared photothermal destruction of cancer cells. *J. Nanopart. Res.* **2015**, *17*, No. 389.
- (33) Hong, Y.; Cho, W.; Kim, J.; Hwang, S.; Lee, E.; Heo, D.; Ku, M.; Suh, J.-S.; Yang, J.; Kim, J. H. Photothermal ablation of cancer cells using self-doped polyaniline nanoparticles. *Nanotechnology* **2016**, *27*, No. 185104.
- (34) Bongiovanni Abel, S.; Molina, M. A.; Rivarola, C. R.; Kogan, M. J.; Barbero, C. A. Smart polyaniline nanoparticles with thermal and photothermal sensitivity. *Nanotechnology* **2014**, *25*, No. 495602.
- (35) Tian, Q. W.; Li, Y. P.; Jiang, S. S.; An, L.; Lin, J. M.; Wu, H. X.; Huang, P.; Yang, S. P. Tumor pH-Responsive Albumin/Polyaniline Assemblies for Amplified Photoacoustic Imaging and Augmented Photothermal Therapy. *Small* **2019**, *15*, No. 1902926.
- (36) Wang, J. P.; Yan, R.; Guo, F.; Yu, M.; Tan, F. P.; Li, N. Targeted lipid-polyaniline hybrid nanoparticles for photoacoustic imaging guided photothermal therapy of cancer. *Nanotechnology* **2016**, *27*, No. 285102.
- (37) Xiang, H. J.; Chen, Y. Energy-Converting Nanomedicine. *Small* **2019**, *15*, No. 1805339.
- (38) Choi, K. Y.; Chung, H.; Min, K. H.; Yoon, H. Y.; Kim, K.; Park, J. H.; Kwon, I. C.; Jeong, S. Y. Self-assembled hyaluronic acid nanoparticles for active tumor targeting. *Biomaterials* **2010**, *31*, 106–114.
- (39) Park, K. E.; Noh, Y. W.; Kim, A.; Lim, Y. T. Hyaluronic acid-coated nanoparticles for targeted photodynamic therapy of cancer guided by near-infrared and MR imaging. *Carbohydr. Polym.* **2017**, *157*, 476–483.
- (40) Huang, G. L.; Huang, H. L. Application of hyaluronic acid as carriers in drug delivery. *Drug Delivery* **2018**, *25*, 766–772.
- (41) Wang, B. J.; Ma, C. J.; Guo, C. J.; Wang, K. L.; Yuan, D. H.; Cheng, H. R.; Liu, M. N.; Fang, L.; Fan, X. X.; Chen, D. Q. Novel Reductive Responsive Chrysin-Oligomeric Hyaluronic Acid Nanomaterials to Curcumin Delivery for Cancer Therapy. *Sci. Adv. Mater.* **2019**, *11*, 1376–1382.
- (42) Mattheolabakis, G.; Milane, L.; Singh, A.; Amiji, M. M. Hyaluronic acid targeting of CD44 for cancer therapy: from receptor biology to nanomedicine. *J. Drug Targeting* **2015**, *23*, 605–618.
- (43) Qiu, J.; Cheng, R.; Zhang, J.; Sun, H. L.; Deng, C.; Meng, F. H.; Zhong, Z. Y. Glutathione-Sensitive Hyaluronic Acid-Mercaptopurine Prodrug Linked via Carbonyl Vinyl Sulfide: A Robust and CD44-Targeted Nanomedicine for Leukemia. *Biomacromolecules* **2017**, *18*, 3207–3214.
- (44) Couzin-Frankel, J. Cancer Immunotherapy. *Science* **2013**, *342*, 1432–1433.
- (45) Liu, Z. G.; Jiang, W.; Nam, J.; Moon, J. J.; Kim, B. Y. S. Immunomodulating Nanomedicine for Cancer Therapy. *Nano Lett.* **2018**, *18*, 6655–6659.
- (46) Jiang, B. P.; Zhang, L.; Zhu, Y.; Shen, X. C.; Ji, S. C.; Tan, X. Y.; Cheng, L.; Liang, H. Water-soluble hyaluronic acid-hybridized polyaniline nanoparticles for effectively targeted photothermal therapy. *J. Mater. Chem. B* **2015**, *3*, 3767–3776.
- (47) Wang, L. P.; Vivek, R.; Wu, W. F.; Wang, G. W.; Wang, J. Y. Fabrication of Stable and Well-Dispersed Polyaniline-Polypyrrolidone Nanocomposite for Effective Photothermal Therapy. *ACS Biomater. Sci. Eng.* **2018**, *4*, 1880–1890.
- (48) Bao, Z. H.; Liu, X. R.; Liu, Y. D.; Liu, H. Z.; Zhao, K. Near-infrared light-responsive inorganic nanomaterials for photothermal therapy. *Asian J. Pharm. Sci.* **2016**, *11*, 349–364.
- (49) Geng, J. L.; Sun, C. Y.; Liu, J.; Liao, L. D.; Yuan, Y. Y.; Thakor, N.; Wang, J.; Liu, B. Biocompatible Conjugated Polymer Nanoparticles for Efficient Photothermal Tumor Therapy. *Small* **2015**, *11*, 1603–1610.
- (50) Shanmugam, V.; Selvakumar, S.; Yeh, C. S. Near-infrared light-responsive nanomaterials in cancer therapeutics. *Chem. Soc. Rev.* **2014**, *43*, 6254–6287.
- (51) Liu, Y. J.; Bhattarai, P.; Dai, Z. F.; Chen, X. Y. Photothermal therapy and photoacoustic imaging via nanotheranostics in fighting cancer. *Chem. Soc. Rev.* **2019**, *48*, 2053–2108.
- (52) Li, Q.; Zhang, D.; Zhang, J.; Jiang, Y.; Song, A. X.; Li, Z. H.; Luan, Y. X. A Three-in-One Immunotherapy Nanoweapon via Cascade-Amplifying Cancer-Immunity Cycle against Tumor Metastasis, Relapse, and Postsurgical Regrowth. *Nano Lett.* **2019**, *19*, 6647–6657.

(53) Ge, R.; Liu, C. W.; Zhang, X.; Wang, W. J.; Li, B. X.; Liu, J.; Liu, Y.; Sun, H. C.; Zhang, D. Q.; Hou, Y. C.; Zhang, H.; Yang, B. Photothermal-Activatable Fe₃O₄ Superparticle Nanodrug Carriers with PD-L1 Immune Checkpoint Blockade for Anti-metastatic Cancer Immunotherapy. *ACS Appl. Mater. Interfaces* **2018**, *10*, 20342–20355.

(54) Chen, Q.; Xu, L. G.; Liang, C.; Wang, C.; Peng, R.; Liu, Z. Photothermal therapy with immune-adjuvant nanoparticles together with checkpoint blockade for effective cancer immunotherapy. *Nat. Commun.* **2016**, *7*, No. 13193.

(55) Vivek, R.; NipunBabu, V.; Rejeeth, C.; Sharma, A.; Ponraj, T.; Vasanthakumar, A.; Kannan, S. Multifunctional nanoparticles for trimodal photodynamic therapy-mediated photothermal and chemotherapeutic effects. *Photodiagn. Photodyn. Ther.* **2018**, *23*, 244–253.

(56) Goldberg, M. S. Immunoengineering: How Nanotechnology Can Enhance Cancer Immunotherapy. *Cell* **2015**, *161*, 201–204.

(57) Sang, W.; Zhang, Z.; Dai, Y. L.; Chen, X. Y. Recent advances in nanomaterial-based synergistic combination cancer immunotherapy. *Chem. Soc. Rev.* **2019**, *48*, 3771–3810.